

# He Scattering from Random Adsorbates, Disordered Compact Islands and Fractal Submonolayers: Intensity Manifestations of Surface Disorder

A.T. Yinnon,<sup>a</sup> D.A. Lidar (Hamburger),<sup>a,b</sup> I. Farbman,<sup>a</sup> R.B. Gerber,<sup>a,c</sup> P. Zeppenfeld,<sup>d</sup>  
M.A. Krzyzowski,<sup>d</sup> and G. Comsa<sup>d</sup>

<sup>a</sup>*Department of Physical Chemistry and The Fritz Haber Center for Molecular Dynamics, The Hebrew University of Jerusalem, Jerusalem 91904, Israel*

<sup>b</sup>*Department of Physics, The Hebrew University of Jerusalem, Jerusalem 91904, Israel*

<sup>c</sup>*Department of Chemistry, University of California - Irvine, Irvine, CA 92717, USA*

<sup>d</sup>*Institut für Grenzflächenforschung und Vakuumphysik, Forschungszentrum Jülich, Postfach 1913, D-52425 Jülich, Germany*

## Abstract

A theoretical study is made on He scattering from three basic classes of disordered adlayers: (a) Translationally random adsorbates, (b) disordered compact islands and (c) fractal submonolayers. The implications of the results to experimental studies of He scattering from disordered surfaces are discussed, and a combined experimental-theoretical study is made for Ag submonolayers on Pt(111). Some of the main theoretical findings are: (1) The scattering intensities from the three disorder classes differ significantly, and can be used to distinguish between them. (2) Structural aspects of the calculated intensities from translationally random clusters were found to be strongly correlated with those of individual clusters. (3) For fractal islands, just as for all surfaces considered here, the off-specular intensity depends on the parameters of the

He/Ag interaction, and does not follow a universal power law as previously proposed in the literature.

In the experimental-theoretical study of Ag on Pt(111), we use experimental He scattering data from low-coverage (single adsorbate) systems to determine an empirical He/Ag-Pt potential of good quality. Then, we carry out He scattering calculations for high coverage and compare with experiments for these systems. The conclusion is that the actual experimental phase corresponds to small compact Ag clusters of narrow size distribution, with partial translational disorder.

## I. INTRODUCTION

The properties of thin metal or semiconductor films on solid substrates are of major theoretical, experimental and technological interest. The structure of these films influences their physical and chemical properties, and these may be of central importance, for example, in the fabrication of electronic devices. The shape of adlayers generally depends on the growth kinetics and the microscopic characteristics of the substrate. Thin films are typically produced by epitaxial growth processes, wherein vapor atoms or clusters are deposited on a substrate.<sup>1,2,3,4,5,6,7,8</sup> Once adsorbed, the adatoms diffuse on the substrate surface, and when reaching short mutual distance they can form stable nuclei, which subsequently grow to clusters or islands by attachment of further adatoms. Nucleation and growth are competing processes, which depend on diffusion of adatoms, stability of the adsorbed clusters, and surface diffusion of these clusters. Therefore, thin film structures contain a wealth of information about microscopic growth processes, and adatom/substrate and adatom/adatom interactions.

Experimental studies have shown that in addition to ordered adlayers, various disordered structures may form. For example on adsorption of Ag on Pt(111) surfaces, at low substrate temperatures and low deposition rates, isolated small clusters may form.<sup>2,3,4,5</sup> Elevation of the surface temperature or lowering of the deposition rate can lead to the growth of fractal islands.<sup>2,3</sup> At even higher temperatures randomly distributed compact islands may form.<sup>2,3,4,5</sup> Therefore, thin films offer an exceptional opportunity for studying two dimensional disordered systems. By investigating the relation between the structure of thin films and their growth processes, valuable information can be obtained about the processes leading to the emergence of different kinds of disorder. This, however, requires techniques for determining the disordered adlayer structure.

Surface morphologies can be probed by scanning tunneling microscopy (STM) or diffraction techniques, such as thermal energy atom scattering (TEAS), low-energy or reflective high energy electron diffraction (LEED or RHEED). Diffraction methods have the property

that in addition to being sensitive to local surface features, they resolve the global surface structure. Accordingly, they provide a better average of the over-all topography than direct imaging techniques, such as STM. Moreover, diffraction readily allows for monitoring adlayer growth in situ and at various temperatures and therefore can easily follow its temporal evolution. For studying surface structure, a technique of great power is Helium atom scattering. It is non-destructive, and He only probes the outer layer. Also, thermal He atom scattering is dominantly elastic. Moreover, since its wavelength is of the order of surface unit cells, it is very sensitive to the local adlayer structure. He atom scattering has successfully been employed in the study of ordered surfaces and surfaces with isolated defects. However, relatively little is known as yet on the manifestations of different kinds of disorder in He scattering patterns. Two of the few experimentally and theoretically studied disordered surfaces are those of substitutionally disordered mixed Xe+Kr monolayers on Pt(111),<sup>9</sup> and translationally disordered small Pt-clusters on Pt(111).<sup>10</sup> It was found that attenuation of the specular peak in He scattering from the surface due to the presence of adsorbates or other defects contains a wealth of information about adatom/adatom interactions, the clustering of adatoms, and 2D vs. 3D epitaxial growth.<sup>10</sup> Also, non-Bragg maxima, e.g., Fraunhofer or rainbow maxima, appear for such systems. These maxima contain information on the microstructure of islands and are sensitive to percolation transitions. Non-specular Bragg peaks appear as well, which contain information on the corrugation of the He/adlayer interaction.<sup>9</sup> The study of randomly adsorbed rare-gas overlayers has the advantage that the interactions between the rare gas atoms and He are well known. In contrast little is known about the interactions in a He/(metal adsorbate)/(metal substrate) system. So far, this has complicated the interpretation of features in the angular scattering patterns, and has made identifying different kinds of disorder difficult.

In this paper, for the first time a comparative He scattering study is undertaken among three major classes of disorder: Translationally random adatoms, translationally random compact islands, and fractal/dendritic submonolayers. These classes are representative of a large proportion of the experimentally reported adlayer structures at submonolayer

coverage.<sup>11</sup> It is thus of fundamental interest to understand the differences in their respective He scattering intensity distributions, and to investigate whether the type of disorder can be identified by a He scattering experiment. In order to carry out this program reliably, we determined the interaction potential between He and a Pt(111) surface with an adsorbed Ag atom. From this we have constructed what we hope is a realistic potential function for He interaction with a *disordered* metal submonolayer. The choice of the Ag/Pt(111) system was motivated by the fact that the He/Pt(111) potential is rather smooth parallel to the surface. Therefore the structures in the scattering patterns are mainly due to the Ag adsorbates. Moreover, the He/Pt(111) belongs to one of the few atom/surface systems for which a fairly reliable empirical potential is available.

The outline of the paper is as follows: Section II describes the experimental and theoretical methods employed, and states the assumptions made in the theoretical part of this work. Section III discusses the scattering from the different disorder classes. In section III C we analyze the experimental scattering data and suggest a morphological identification of the disordered phase present on the surface. Concluding remarks are presented in section IV.

## II. SYSTEMS AND METHODS

The adlayer structures studied here theoretically are:

1. Full Ag monolayer.
2. Single adsorbed Ag atom.
3. Isolated small compact cluster (henceforth SCC).
4. Ag adatoms randomly adsorbed on a lattice.
5. SCCs of Ag randomly adsorbed on a lattice.
6. Ag adatoms completely randomly and continuously distributed (Ag adatoms can be arbitrarily close).

- 7. Large compact Ag islands.
- 8. Fractal islands of Ag atoms.

(1) and (2) are important as a reference, and for developing potentials. All other cases were chosen as representing important types of disorder. In all cases, the adsorbates are on a Pt(111) surface. In the case of randomly adsorbed Ag adatoms one would expect to observe system (4) and not the idealized system (6). However, calculations for the latter structure leads to additional insight into angular scattering patterns.

### A. Experimental Methods

The experiments were performed in a high resolution UHV helium scattering apparatus with a nominal base pressure  $< 10^{-10}$  mbar. The system is equipped with a commercial Knudsen cell by means of which high purity (99.999%) silver can be evaporated onto the Pt(111) sample at a rate between  $10^{-1}$  and  $10^{-4}$  monolayers per second. The Pt(111) sample was cleaned by repeated cycles of heating in an oxygen atmosphere ( $10^{-6}$  mbar) at 750K, sputtering with 1 keV Ar-ions followed by short annealing at 1250K. The sample is mounted on a manipulator which allows the crystal to be rotated around its three principal axes. In addition, the total angle  $\chi = \theta_i + \theta_f$  of the incident and outgoing He-beam can be varied between  $60^\circ$  and  $120^\circ$  by rotating the detector. By means of a liquid helium cryostat the sample can be cooled to 20K and by concomitant heating by electron bombardment the surface temperature can be set and held constant at any value between 20K and 1250K.

The experiments reported here (e.g., Fig.1) involve two different modes of operation of the He-scattering apparatus. In the first mode, the specularly scattered He-intensity is recorded during the deposition of silver at a constant rate. From the initial slope (extrapolated towards silver coverage  $\Theta \rightarrow 0$ ) the scattering cross-section of the Ag-nuclei initially formed on the surface are obtained. From a detailed analysis of the shape of the deposition curves, we can infer that at the temperature of 38K at which the data in Fig.1 were taken these

initial Ag nuclei are individual Ag atoms randomly distributed on the Pt(111) surface. The initial slope of the He-intensity curve, therefore, directly yields the He cross section  $\Sigma(k_z)$  (as defined by Eq.(6) below), where  $k_z = k \cos(\theta_i)$  is determined by the wavevector  $k$  of the incident He beam, related to its energy by  $E = \hbar^2 k^2 / (2m)$ .  $\theta_i = \theta_f$  (specular scattering) denotes the incident and outgoing angle of the He beam measured against the surface normal. To measure the dependence of the cross section  $\Sigma$  on  $k_z$ , either the total scattering angle  $\chi = \theta_i + \theta_f$  or the energy of the incident He beam has to be varied. We have chosen the second option which, in practice, we achieve by varying the nozzle temperature from liquid nitrogen temperature to above room temperature at constant total scattering angle  $\chi = 90^\circ$ . This temperature variation corresponds to a change of the energy  $E$  from 18 to 90 meV, i.e., from  $k_z = 4.15 \text{ \AA}^{-1}$  to  $9.28 \text{ \AA}^{-1}$ .

The second type of experiment is the analysis of diffraction profiles as shown, e.g., in Fig.8. Here, the He-intensity is recorded as a function of the *parallel* wavevector transfer  $\Delta \vec{K}$ . In the present case, the incident and outgoing beams lie in the same plane as the surface normal (*in plane scattering*) and  $\Delta K = k(\sin \theta_f - \sin \theta_i)$ . The azimuthal orientation of the scattering plane relative to the surface crystallographic directions can be varied by rotating the crystal around its surface normal. In Fig.8 the surface was oriented along the  $[11\bar{2}]$ -direction (i.e., the direction along which the first order Bragg peaks of the hexagonal substrate lattice are expected).

Our scattering apparatus is equipped with a time-of-flight (TOF) spectrometer allowing to separate the elastic from the inelastically scattered He intensity by counting only those He-atoms within a narrow energy window of about 0.5meV centered around the incident beam energy. In this way, even the very small elastic signals away from the Bragg peaks can be discriminated. As shown in the next sections, these elastic features provide important information on the surface morphology.

All the experiments reported here were conducted at *low* temperatures,  $T = 38K$ . As already mentioned, this ensures that small silver clusters are formed as a consequence of the limited mobility of the Ag adatoms on the Pt(111) surface. Although similar in size and

distribution, these low-temperature structures should not be confused with those obtained after depositing or annealing Ag at *high* surface temperature,  $T \geq 620\text{K}$ .<sup>2,3,4</sup> At these elevated temperatures, the Ag atoms are embedded into the topmost Pt(111) layer forming small, stable clusters as a consequence of the surface strain.<sup>4,12</sup> Instead, the low temperature structures presented here are diffusion limited aggregates composed of Ag atoms adsorbed *on top* of the Pt(111) surface. A detailed account on the difference of these two configurations will be given in a forthcoming paper.<sup>13</sup>

## B. Theoretical Methods

In modeling the substrate, we assumed a flat supporting surface. Indeed, the He/Pt(111) equipotential surface is rather smooth, leading to very little off-specular scattered He.<sup>14</sup> However, due to the lattice misfit of about 4% between Ag and Pt,<sup>13,15</sup> the assumption of a flat Pt(111) surface is only a reasonable first approximation. In addition, in all of our calculations we assume the Ag/Pt(111) system to be rigid. Note that experimentally the inelastic contribution can be separated by a TOF spectrometer. As for elastic scattering, results of calculations using a rigid, non-vibrating surface system should be useful at least for studying the main qualitative features. Moreover, for diffraction scattering from crystalline surfaces, the effect of surface vibrations on the scattering intensities can be represented approximately by a simple Debye-Waller factor.<sup>16,17,18</sup> A similar description should be successful for the angular intensity distributions obtained in scattering from an adlayer.

### 1. Kinetic Monte Carlo Simulations of Diffusion Limited Aggregates

We outline here the methods used to simulate the compact and fractal Ag islands (systems (7,8); Figs.6,7). There is an extensive literature on the modeling of adsorption, diffusion and aggregation processes on homogeneous surfaces.<sup>19</sup> To produce realistic arrangements of adatoms on the surface we adopted the Kinetic Monte Carlo (KMC) method.<sup>20</sup> The Pt(111) surface was simulated as a hexagonal lattice of  $100 \times 100$  unit cells with periodic boundary



conditions. As for the lateral interaction between adsorbed particles, the assumptions made are critical for the shape and size of the final clusters formed. We assumed that the interactions between two adsorbates depend on the number of their nearest neighbors,  $n_{NN}$ . Thus the energy of a particle in a given configuration is:

$$E(n) = E_0 + n_{NN} \epsilon \quad (1)$$

where  $E_0 = 5.2\text{kcal/mole}$  is the activation energy for diffusion at zero coverage, and  $\epsilon = 5.0\text{kcal/mole}$  is the nearest neighbor interaction energy. No values were available for the  $\epsilon$  parameters for Ag on Pt(111). Therefore, we adopted the values given by Rosenfeld et al.<sup>5</sup> for Pt adsorbed on Pt(111). These values, while not more than semiquantitatively valid, should at least allow for the formation of plausible aggregates.

The diffusion of adatoms was modeled by random walks over nearest neighbor sites. The hopping rate, i.e., the transition probability per unit time, of a particle from site  $i$ , where it has  $n_i$  nearest neighbors, to a neighboring site with  $n_f$  nearest neighbors, is taken as

$$\omega_{i \rightarrow f} = \nu e^{-E(n_i)/(kT)} = \omega_0 e^{-n_i \epsilon/(kT)} \quad (2)$$

where  $\omega_0 = \nu \exp[-E_0/(kT)]$  is the hopping frequency of an “isolated” particle;  $\tau_0 = 1/\omega_0$  is the average time interval between successive moves on the bare (zero coverage) surface. Since there is an uncertainty in our data regarding the values of the activation energy  $E_0$  and the interaction energy  $\epsilon$ , it must be commented that there is a resulting uncertainty in the temperature scale: Changing  $T$  at constant  $E(n)$  is equivalent to changing  $E(n)$  at constant  $T$ . Note further that according to Eq.(2), the transition rate depends only on the initial state. A possible dynamical interpretation of this model, originally suggested by Uebing and Gomer,<sup>21</sup> is that the rate of the transition from state  $i$  to state  $f$ , is governed by the energy difference between the initial state and the transition state. The same is of course true also for the reverse process (with the final state replacing the initial state), so that detailed balance is obeyed. We note that a situation where a rate depends on the gap between any given initial state and the transition state holds widely for many activated

rate processes. Hopping diffusion involves overcoming a barrier between the initial and final configurations and therefore the model seems most reasonable here. The KMC simulations were performed using the time-dependent Monte-Carlo scheme.<sup>20</sup> In this scheme, instead of randomly choosing particles and accepting or rejecting moves according to the given transition probabilities (as in the “traditional” MC simulations), one performs a move in any attempt, and propagates the time accordingly. More explicitly, we first calculate the average transition rate  $\langle r \rangle = 1/\langle \omega_{i \rightarrow f} \rangle$  out of state  $i$ , then randomly sample a given  $i \rightarrow f$  move with probability  $\omega_{i \rightarrow f} / \sum \omega_{i \rightarrow f}$  and, finally, perform this move and record the time elapsed as  $\Delta t = 1/\langle r \rangle$ . Further details about this procedure can be found elsewhere.<sup>19,20</sup>

The simulation starts with two particles diffusing on the surface until a third particle adsorbs. This period is typically 0.05 sec (for simulating an adsorption rate of 1ML/500sec), corresponding to about  $10^6$  MC steps at room temperature. Then the three particles diffuse, a fourth one adsorbs, and so on until the desired coverage is obtained. The configurations attained are not at equilibrium, but reach a steady state after some time duration, when the adsorption is terminated. The true equilibrium state corresponds most probably to a segregated phase, with one large compact island formed by all the adsorbates. Both the compact and the fractal clusters of Figs.6,7 were generated according to this procedure, differing only in the respective temperatures of 500K and 200K.

## *2. He Scattering Calculations*

The scattering intensities were calculated using the Sudden Approximation (SA),<sup>18,22,23,24,25</sup> which has proved very useful in studies of atom scattering from defects<sup>26</sup> and from substitutionally disordered rare-gas monolayers.<sup>9</sup> On the basis of the experience gained with the SA, including tests against numerically exact calculations for several model systems,<sup>27</sup> we estimate that at least the main predictions of the SA calculations should be reliable for the systems studied here.

The SA takes the following form for the systems studied below. Consider a particular

(static) configuration  $\vec{r} = \{\vec{r}_1, \dots, \vec{r}_N\}$  of a disordered adlayer system consisting of  $N$  atoms with  $\vec{r}_i$  denoting the position of atom  $i$ . The angular intensity distribution for He scattered from this adlayer involves an average over all configurations pertinent to the disorder:<sup>23,24</sup>

$$I(\Delta\vec{K}) = \frac{1}{A^2} \left\langle \left| \int \int e^{i\Delta\vec{K}\cdot\vec{R}} e^{2i\eta_{\vec{r}}(\vec{R})} d\vec{R} \right|^2 \right\rangle. \quad (3)$$

In this expression  $\Delta\vec{K} = \vec{K}' - \vec{K}$  is the wavevector transfer of the He parallel to the surface, where  $(\vec{K}, k_z)$  is the incident wavevector, and  $(\vec{K}', -k_z)$  the final wavevector of the scattered He atom;  $\vec{R} = (x, y)$  denotes the coordinates of the He atom in the surface plane;  $A$  is the area of the surface over which the integration in Eq.(3) is performed;  $\langle \dots \rangle$  denotes the average over all configurations of the quantity in parenthesis;  $\eta_{\vec{r}}(\vec{R})$  denotes the phase shift for He scattering for an adlayer having a configuration  $\vec{r}$ . The phase shift is given in the WKB approximation by<sup>22</sup>

$$\eta_{\vec{r}}(\vec{R}) = \int_{\xi(\vec{R})}^{\infty} dz \left( \left[ k_z^2 - 2m V_{\vec{r}}(\vec{R}, z)/\hbar^2 \right]^{1/2} - k_z \right) - k_z \xi(\vec{R}), \quad (4)$$

where  $m$  is the mass of the He atom and  $z$  denotes the distance of the He atom from the surface plane;  $V_{\vec{r}}(\vec{R}, z)$  is the interaction potential between the He atom at position  $(\vec{R}, z)$ .  $\xi(\vec{R})$  in Eq.(4) is the classical turning point for the He atom when colliding with the surface at the lateral position  $\vec{R}$ , i.e.,  $\xi(\vec{R})$  is the  $z$  value for which

$$(\hbar k_z)^2 - 2m V_{\vec{r}}(\vec{R}, z) = 0 \quad (5)$$

### 3. The Interaction Potential

To determine the interaction of He atoms with the Pt(111) surface with a single adsorbed Ag atom, we calculated the attenuation of the specular peak with incident He energy. This attenuation is closely related to the cross-section of the adatom. The relation between the cross-section  $\Sigma$  and the specular intensity  $I$  for scattering from random *isolated* adatoms is:<sup>26,28</sup>

$$\Sigma = \frac{1}{I_0} \lim_{\Theta \rightarrow 0} \frac{dI}{d\Theta}, \quad (6)$$

where  $I_0$  represents the specular scattering intensity from the clean Pt(111) surface,  $n$  is the number of sites per unit cell, and  $\Theta$  the adatom coverage. The parameter  $\Sigma$  in Eq.(6) can be interpreted as the cross-section of a single adatom. Indeed, Eq.(6) is only valid when the cross-section of different atoms can be viewed as non-overlapping.  $\Sigma$  is very sensitive to the interaction potential. Therefore, we tried to find a potential that is capable of reproducing the experimentally observed changes in the specular scattering. We assumed the following general form for the interaction potential between He and the Pt(111) surface with an adsorbed Ag atom:

$$V_{\text{He/Ag/Pt(111)}} = V_{\text{He/Pt(111)}} + V_{\text{He/Ag}}, \quad (7)$$

where  $V_{\text{He/Pt(111)}}$  is the interaction potential of He with the clean Pt(111) surface. A He-Pt Morse potential,

$$V(z) = D_e \left( e^{-2\alpha(z-z_m)} - 2e^{-\alpha(z-z_m)} \right) \quad (8)$$

for this interaction<sup>29</sup> is available in the literature, with  $D_e = 7.86\text{meV} = 2.89 \times 10^{-4}\text{a.u.}$  and  $\alpha = 0.98\text{\AA}^{-1} = 0.52\text{a.u.}$ <sup>30</sup>  $V_{\text{He/Ag}}$  is the interaction between He and an isolated adsorbed Ag atom. We modeled this interaction with a Lennard-Jones potential, and changed its parameters until the potential could reproduce the dependence of the experimental cross-section on the incidence energy of the He atom. This procedure also yielded the value of  $z_m = 11.46\text{a.u.}$  in the Morse potential. The high sensitivity of this fit to the parameter values is the source of our confidence in the semiquantitative reliability of the potential.

For the interaction between He and multiple adsorbed Ag atoms, we assumed pairwise interactions for the He atom with the adsorbed Ag atoms, i.e.,  $V_{\text{He/Ag}}$  in Eq.(7) is replaced by  $\sum_i V_{\text{He/Ag}}(r_i)$  where  $r_i$  is the distance of the He from the  $i^{\text{th}}$  Ag atom. The pairwise additive potential for the interaction with a collection of Ag atoms is expected in general to be no better than a first approximation. We estimate, however, that it is sufficient in accuracy for our purpose here.

### III. RESULTS AND DISCUSSION

#### A. He Interaction Potential with Pt(111) and adsorbed Ag

Specular scattering intensities were measured as a function of He incidence wavenumber for a *single* adsorbed Ag atom. Using these values in Eq.(6) provided us with the experimentally determined cross-sections, shown in Fig.1. Experimental constraints detailed in Sec.II A limited the range of incident He wavenumber values. Subsequently, we attempted to fit the experimental cross-section data by finding an optimal set of  $C_{12}$  and  $C_6$  values for the He/(adsorbed Ag atom) Lennard-Jones 6-12 potential

$$V_{\text{He/Ag}} = \frac{C_{12}}{r^{12}} - \frac{C_6}{r^6}, \quad (9)$$

with which the specular intensities were calculated from Eq.(6). By adopting this trial and error approach, we found that the experimental values are best reproduced with the following Lennard-Jones parameters:  $C_{12} = 6.33 \times 10^6$  a.u. and  $C_6 = 29.0$  a.u. This leads to  $r_{eq} = (2C_{12}/C_6)^{1/6} = 4.6\text{\AA}$  and  $V(r_{eq}) \approx 0.9\text{meV}$ . A comparison between the experimental and theoretical values is presented in Fig.1. We found the fit to be very sensitive to these parameters, suggesting that our empirically determined potential models the long range attractive and the short range repulsive interactions well, and its accuracy is mainly limited by the experimental uncertainty.

#### B. Angular Scattering Patterns from Disordered Overlayers

The results will be outlined by examining the angular distributions of each of the disorder classes, and comparing among them. In each case where random ensembles are discussed, we averaged over 30 configurations.

### 1. Scattering from a Full Monolayer (system (1))

To evaluate the influence of surface disorder on He scattering, we first calculated for reference the angular intensity pattern for He scattered from a *completely ordered monolayer* of Ag on Pt(111), i.e., for a silver coverage  $\Theta = 1$ . (The issue of incommensurability does not arise here because we take the Pt(111) surface to be flat – Eq.(8)). The incident perpendicular He momentum is  $3\text{bohr}^{-1} = 5.67\text{\AA}^{-1}$  (For the other calculations presented below, we assumed the same incident momentum.) The result, presented in Fig.2, shows strong first order Bragg peaks along with the specular peak. The very weak background intensity is due to finite grid effects. Note that our calculations, based on a pairwise additive potential, probably give the effect of a too corrugated surface (hence diffraction stronger than the real one) since the smoothing role of the conduction electrons is not included in the interaction.

### 2. Scattering from Single Clusters: Adatom and Small Compact Cluster (systems (2),(3))

The simplest deviation from perfect order is the introduction of a single defect. Such defects, namely a single Ag adatom and SCC are the subject of this section. In subsequent sections gradually more disordered systems will be considered.

The dashed lines in Figs.3,4 present the scattering results from a single adatom and an SCC (heptamer) respectively. Despite their quantitatively different appearance, the scattering patterns share some important qualitative features:

*a. Specular Peak:* The sharp specular peak is due to He scattered from uncovered Pt(111) surface areas, where the He/Pt(111) potential is not influenced by the defect. The flatness of this potential across the unperturbed surface results in almost perfect mirror scattering.

*b. Broadening of the Specular Peak:* Immediately below the specular “spike” a shoulder appears, which is clearly wider in the single adatom case. In other words, the broadening of the specular peak is inversely related to the cluster size.

*c. Off-Specular Peaks:* A series of rather broad, off-specular diffraction features follows the specular broadening. The interesting feature is their spacing, which is larger for the single adatom. Again, this spacing in reciprocal space is inversely related to the cluster size. For a detailed quantitative analysis of this issue see Ref.[10]. Here it will suffice to mention that the peak structure, as well as the specular broadening, can be satisfactorily explained in terms of scattering from a hard hemispherical object of radius  $d$ . The resulting *Fraunhofer* diffraction intensities are given by:<sup>31</sup>

$$I(\phi) \propto \left| \frac{(1 + \cos \phi) J_1(k d \sin \phi)}{\sin \phi} \right|^2, \quad (10)$$

where  $\phi$  is the scattering angle,  $J_1$  denotes the Bessel function of first order, and  $k$  is the incident wavenumber. The parameter  $d$  can be interpreted as the radius of the scattering cross-section. Indeed, we found using Eq.(10), that for scattering from an isolated heptamer (Fig.4), the Fraunhofer interferences are those characteristic for an average island scattering cross-section of three nearest-neighbor Ag atoms.

Another mechanism at work in the scattering from defects is *rainbow scattering*, in which the positions of the peaks are determined by the inflexion points of the equipotential surface.<sup>25,18</sup> For an extensive treatment of this issue in the heptamer case, see Ref.[10].

### 3. Scattering from Adatoms and SCCs Randomly Adsorbed on a Lattice (systems (4),(5))

A natural transition to more complex disorder is obtained by considering a collection of clusters, randomly adsorbed on the hexagonal lattice. A system like this can be formed in realistic conditions when gas phase Ag atoms are deposited on a cold Pt(111) surface, such that the Ag mobility is very small.<sup>2,3,4,5</sup> Scattering from such *translationally random* systems is the subject of the present section.

The results for a system of single adatoms and SCCs at 15% coverage are presented as the solid lines in Figs.3,4. Let us enumerate the central features:

*a. Specular and Bragg Peaks:* The sharp specular peak is as usual an indication that significant portions of the Pt(111) surface remain flat. In addition one observes strong

first and second order Bragg peaks at multiples of  $2\pi/a$  ( $a = 2.77\text{\AA}$  is the Pt(111) lattice constant). What is their origin? It is not the underlying *flat* Pt(111) surface, as proved by the absence of Bragg peaks in the case of the individual defect systems of Figs.3,4. Nor is it the small (111) plateau on top of the SCCs (see inset of Fig.4), since the Bragg peaks are observed also for the adatom system, which has no such structure. Thus these peaks can only be the result of the strong corrugation induced by the presence of the Ag adatoms and clusters on the *lattice*. This must be so in spite of their *random* positions on this lattice. Since the Bragg peaks are robust and their intensities are comparatively high ( $\sim 10^{-3}$  relative to specular), they are easily measurable. In addition, they yield to a simple theoretical description, and thus are attractive candidates for the calibration of a simple model potential from experimental data.

*b. Similarity to Single Cluster and Effect of Disorder:* Perhaps the most striking result from the present calculations is the close (qualitative) resemblance between the intensity distributions from the single clusters and their random counterparts. This can be seen very clearly in Figs.3,4, where the distributions are slightly offset for clarity. As is especially conspicuous in the SCC case (Fig.4), there is a one-to-one correspondence between essentially every (broad) off-specular peak in the single and random case, respectively. The effect of the randomness seems to be limited to a modification of the single-cluster intensity distribution by the addition of noise. In the previous section we identified the principal cause for the peak structure in the scattering from a single cluster to be Fraunhofer scattering. This, then, must also be the dominant mechanism in the scattering from the random systems. The Fraunhofer mechanism is sensitive to *local* surface details, through the cross-section of the individual cluster [Eq.(10)]. Since this is a feature of the adlayer which is not expected to change significantly in the transition to an ensemble, the similarity agrees with intuition. But why does the randomness have such little effect? This can be understood qualitatively as follows: For a regular *super-lattice* of islands, one would expect a set of Bragg peaks at multiples of the inverse super-lattice constant. For a random set of islands, as in the present



case, such long-range translational order is not present, and the only order that remains in the system is the structure of the individual islands and the discreteness of the underlying lattice giving rise to the Bragg peaks at the Pt positions. Hence this is the only coherent contribution (though the Fraunhofer or rainbow mechanisms) to the intensity spectrum. The effect of the disorder is then reduced to the addition of noise. In the next section we investigate what happens when even the pinning due to the underlying substrate lattice is lost.

#### 4. *Scattering from a Fully Random Adatom System (system (6))*

In the previous section we considered a random adatom system on a lattice. Here we consider the same system of randomly located adatoms, with the lattice constraint removed. Thus, each Ag adatom is located completely randomly, as if the Pt(111) surface were perfectly smooth. Although this system is rather artificial, it removes the distance length scale between the atoms, which the lattice implies. Consequently in this model, adatoms can be “merged” into each other into statistically allowed structures. This non-lattice system is amenable to analytical modeling, as discussed below.

The scattering results from this system are presented in Fig.5, for a system of 15% coverage Ag on Pt(111). The scattering intensity is very similar to that obtained for the lattice system of Fig.3. The broadening of the specular peak is essentially identical, and the decay of the intensity beyond the broadening is the same apart from the oscillations absent in Fig.5. These oscillations, then, can most likely be identified as the result of Fraunhofer interference, whose effect is suppressed due to the loss of adatom identity in the present case.

Another sharp feature evidenced in Fig.5 is the presence of *two distinctly different slopes* dominating the intensity distribution. The slope discontinuity occurs at about  $\Delta K^* = 3\text{\AA}^{-1}$ , and is an indication that there exist two important structural regimes on the surface: The individual cluster, and the long-range translational randomness. Why  $3\text{\AA}^{-1}$ ? The answer

can be found in the single adatom scattering intensity of Fig.3:  $3\text{\AA}^{-1}$  is exactly the point where the specular broadening reaches a minimum, and the Fraunhofer interference pattern takes over (the actual value of course depends on the cluster radius). One would expect that the small  $\Delta K$  ( $< \Delta K^*$ ) regime corresponds to the long range surface-structure, and vice versa. To check this, we repeated the calculation with a “harder” He/Ag potential ( $C_{12} = 3.0 \times 10^7 \text{a.u.}$ ,  $C_6 = 7.0 \text{a.u.}$ ), which enhances the effect due to the individual cluster structure. The result is presented in the right inset in Fig.5. The slope discontinuity at  $\Delta K^*$  is even more pronounced here, and oscillations reminiscent of the on-lattice system are observed as well for  $\Delta K > \Delta K^*$ . The reason is that this harder potential effectively increases the local surface corrugation; consequently the surface is rougher and leads to increased high-angle scattering. Thus changes in the He/Ag potential strongly affect the intensity distribution for *large*  $\Delta K$  values, which therefore contain important information on the He/adsorbate potential. Furthermore, by studying the large  $\Delta K$  regime, a He scattering experiment can be used as a tool to measure adatom electron densities, which are related to the He/adsorbate potential.<sup>32</sup> It is clear from the above analysis that the short-range structure, manifested by the local corrugation (and controlled by the hardness of the potential), appears in the *large*  $\Delta K$  regime. However, the small  $\Delta K$  behavior is identical even for the hard-potential case. This proves that this regime is determined exclusively by the long-range structural features of the surface, as indeed expected.

The question arises whether we can isolate the long-range effect of the surface disorder ( $\Delta K < \Delta K^*$ ) from that of the interaction with a single defect. In order to completely isolate the effect of the translational randomness of the clusters, we introduce a highly simplified *two-state* model (TSM), in which every adatom is represented by a cylinder of height  $h$  and a diameter  $d$ , and the adatoms are completely randomly located. Here  $h$  is the height of an adatom above the Pt(111) surface and  $d$  is the diameter of the adatom scattering cross-section. The adatoms are assumed to be fully mutually penetrable. The resulting system may be considered as a *two-phase random medium*, in the sense that the underlying

surface and the incomplete layer of tops of islands are two separate phases from the point of view of the incident He beam. This approximation is reasonable for systems of metal atoms adsorbed on metal surfaces, because the corrugation of metal islands is extremely weak. By representing the adatoms as structureless cylinders, we capture only the *global* features of the system, neglecting its local structure, and can thus hope to reproduce only those features of the spectrum which result from the underlying random scattering system.

An outline of the solution of this TSM for the intensities is given next; for additional details see the appendix. For scattering from a hard island on a hard surface, the general expression for the scattering intensity [Eq.(3)] becomes:

$$I(\Delta\vec{K}) = \frac{1}{A^2} \int d\vec{R}_1 \int d\vec{R}_2 e^{i\Delta\vec{K}\cdot(\vec{R}_1-\vec{R}_2)} \langle e^{2ik_z Z(\vec{R}_1, \vec{R}_2)} \rangle, \quad (11)$$

where

$$Z(\vec{R}_1, \vec{R}_2) = \xi(\vec{R}_2) - \xi(\vec{R}_1) \quad (12)$$

and  $\xi(\vec{R})$  is the classical turning point at  $\vec{R}$  for a hard surface, and

$$\langle e^{2ik_z Z(\vec{R}_1, \vec{R}_2)} \rangle = \int dz e^{2ik_z z} f_Z(z; \vec{R}_1, \vec{R}_2). \quad (13)$$

Here  $f_Z(z; \vec{R}_1, \vec{R}_2)$  is the probability density of observing a height difference  $z$  between two points located at  $\vec{R}_1$  and  $\vec{R}_2$  on the surface. The problem of obtaining  $I(\vec{Q})$  therefore reduces to the evaluation of  $f_Z(z; \vec{R}_1, \vec{R}_2)$ . In the case of realistic shape functions for the island, the evaluation of  $f_Z$  is a very hard problem, because it requires to take into account the 3D shapes of all possible cluster types. The TSM renders the problem of finding  $f_Z$  tractable, at the expense of losing certain details in the long-range part of the real intensity distribution.

Rewriting Eq.(13) for the case of a stepped surface, we obtain:

$$\langle e^{ik_z Z(\vec{R}_1, \vec{R}_2)} \rangle = \sum_j e^{2ik_z z_j} \text{Pr}(z_j; \vec{R}_1, \vec{R}_2) \quad (14)$$

where the sum is over all possible height differences, and  $\text{Pr}(z_j; \vec{R}_1, \vec{R}_2)$  is the probability to observe a given height difference between the points  $\vec{R}_1$  and  $\vec{R}_2$ . In the present case

$z_j = 0, \pm h$ . The problem now reduces to evaluating  $\text{Pr}(z_j; \vec{R}_1, \vec{R}_2)$ . Our evaluation for randomly adsorbed islands is presented in the appendix, and shows that for this case the scattering intensity Eq.(11) becomes:

$$I(\Delta\vec{K}) = c_1(\rho d^2, 2k_z h, A)\delta(\Delta\vec{K}) + c_2(\rho d^2, 2k_z h, d^2/A) \left[ g(\Delta K d, \rho d^2) + \frac{J_1(\Delta K d)}{\Delta K d} \right]$$

$$g(\alpha, \beta) = \int_0^1 J_0(\alpha S) e^{\frac{1}{2}\beta(\cos^{-1} S - S\sqrt{1-S^2})} S dS, \quad (15)$$

where  $J_1$  is the modified Bessel function of order 1, and  $\rho$  is the adsorbate density. The factors  $c_1, c_2$  are independent of  $\Delta\vec{K}$ . The important point to notice about Eq.(15) is that apart from a specular term, it is composed of a term due to a *single* cylindrical adatom (the  $J_1$  term – compare to Eq.(10)), and a new term ( $g$ ), which incorporates the effect of the surface disorder. As can be seen in the left inset in Fig.5, the effect of the disorder term is very significant: It completely dominates the small  $\Delta K$  regime compared to the single adsorbate term. In particular the *slope* in this  $\Delta K$  range is controlled almost exclusively by the disorder term (in contrast to the *width*, which was previously shown to be determined by the radius of the islands). This explains the universality of this slope in all the random models considered above.

Next, Eq.(15) was applied to study the quantitative aspects of the small  $\Delta K$  region. The height  $h$  has mainly the effect of an overall intensity factor. Since one cannot expect the crude TSM to correctly predict the intensities, we shifted the intensity curves in the  $(\Delta K, \log(I))$  plane, and focused on the effect of changing the cylinder diameter  $d$ . At the incidence wavenumber of  $k_z = 3.0 \text{ bohr}^{-1} = 5.7 \text{ \AA}^{-1}$ , Fig.1 predicts a cross-section of  $\sim 140 \text{ \AA}^2$ , i.e., a diameter of  $\sim 5a$ . In Fig.5 we show the TSM prediction for  $d = 5a, 10a$ . The effect of increasing the diameter is to flatten the intensity. The  $d = 5a$  case clearly underestimates the intensity, whereas for  $d = 10a$  there is good quantitative agreement in the small  $\Delta K (< \Delta K^*)$  regime. Thus, not surprisingly, the TSM does not offer good quantitative agreement for realistic parameter values. However, the agreement improves when the TSM is compared to the “hard-potential” case (see inset in Fig.5), which is consistent with its formulation as a hard-wall model.

In conclusion, the relative success of the TSM in representing the small  $\Delta K$  regime (as well as its failure to agree with the large  $\Delta K$  region!), demonstrates convincingly that the properties of the long-range structure of the disordered surface can be found from the quantitative analysis of this regime.

### 5. Scattering from Large Compact Islands (system (7))

In this and the next section we discuss the scattering from yet more complex, stochastic systems: those created by the Kinetic Monte Carlo algorithm described in Sec.II B 1. A typical configuration of the large, quasi-compact islands formed at 500K is shown in the inset in Fig.6. Note that periodic boundary conditions are employed. It is not our purpose here to obtain a quantitative description of the structure of these islands from the scattering intensities. Instead, we will limit ourselves to a discussion of some of the main features of the intensity distribution, and contrasting them with those characteristic of the systems studied above.

*a. Broadening of the Specular Peak:* Among all the systems discussed so far, the specular broadening observed in Fig.6 is the smallest. This corresponds, as expected, to the large area of the individual islands. The observed width is  $\sim 0.3\text{\AA}^{-1}$ , in agreement with an average island diameter of 13-17 $a$  obtained in our KMC simulations. Thus, as indeed obvious, the specular broadening can be used experimentally to find the average diameter of randomly adsorbed islands.

*b. Broadening of the Bragg Peaks:* In contrast to the case of translationally random adatoms or SCCs, there is little off-specular structure in Fig.6. The exception are the Bragg peaks, whose existence in the present case is not surprising, considering the large island surface area, which has the underlying Pt(111) lattice corrugation. However, the new feature is the *broadening* of the Bragg peaks. The broadening is roughly half that of the specular peak. This phenomenon is reminiscent of Fraunhofer interference of light transmitted through a grating. Indeed, roughly speaking, the uncovered surface area between

the islands can be thought of as a slit pattern. The kinetics governing the formation of the islands leads to depletion zones, or an *effective* repulsion between them (since they cannot overlap), thus inducing a degree of regularity in this pattern, which can yield the Fraunhofer broadening. Note that this is different from the Fraunhofer scattering by a hemispherical object described by Eq.(10), which is responsible for the specular peak broadening and the “humps” at  $\Delta K = \pm 1.5, 3.0 \text{ \AA}^{-1}$ . The irregularity in “slit” sizes and orientations, as well as to a lesser extent their positions, both due to the inhomogeneity of island sizes and separation, is responsible for the added noise.

### *6. Scattering from Fractal Islands (system (8))*

In this section we discuss the scattering results from the last model system considered in this work: the dendritic/fractal structures formed by the KMC simulations at 200K. The interest in such structures hardly needs recapitulation. The averaged scattering intensities, as well as a typical configuration, are shown in Fig.7. This configuration is rather reminiscent of STM results on Pt/Pt(111)<sup>11,33</sup> and Ag/Pt(111)<sup>34</sup> obtained under similar conditions. The fact that these systems are indeed fractal over a number of orders of magnitude of resolution-observation, is discussed in detail elsewhere.<sup>35</sup>

Interestingly, in spite of the non-negligible surface area of the clusters, there is apart from weak first order Bragg peaks almost no trace of interference in Fig.7. This is in agreement with the characterization of a fractal as an object with no typical length scale between physical lower and upper cutoffs. Indeed, our “fractals” are composed of a large variety of clusters of different sizes (dimers, trimers and larger clusters), which generally are somehow connected. Each of these clusters contributes Fraunhofer peaks at its typical length scale. The net effect is to smear out these peaks into a relatively smooth decline of the intensity. However, since the fractal clusters are all finite in size, their average radius *is* reflected in the scattering distribution, as the by now familiar specular broadening. Apart from this, the absence of a typical length scale (above the lower cutoff *a*) results in that there is essentially

no structure left in the intensity distribution.

As for the intensities at  $\Delta K$  beyond the broadening, we observe that the decline of the angular intensity with  $\Delta K$  for fractal islands is very similar to that for randomly adsorbed adatoms (Fig.3), and quite similar to the average decline for SCCs and large compact islands (Figs.4,6). Furthermore, as mentioned earlier, this dependence is determined by the He/Ag/Pt(111) interaction potential. Nevertheless, we attempted to fit the intensities both before and beyond the broadening ( $|\Delta K| > 2\text{\AA}^{-1}$ ) by a potential-independent power-law, following Ref.[36]:

$$I(\Delta K) \propto \Delta K^{D-4}. \quad (16)$$

Here  $D$  is the fractal dimension. The right inset of Fig.7 shows the result of this fit for both positive and negative  $\Delta K$  (the latter were reflected), after elimination of the specular and Bragg peaks. The result is a slope of  $-1.84 \pm 0.03$  for  $|\Delta K| < 2\text{\AA}^{-1}$ , and  $-1.62 \pm 0.06$  for  $|\Delta K| > 2\text{\AA}^{-1}$  over a total range of slightly less than one decade, with respective regression coefficients of -0.99 and -0.90. If these slopes were used in accordance with Eq.(16), the fractal dimension would be  $D > 2$ . Clearly, this cannot be for our planar sets, so that we conclude that the procedure suggested by Eq.(16) is *not* generally valid for the determination of fractal dimensions from He scattering data. A further reason is that the intensities beyond the specular broadening depend strongly on the hardness of the potential. For example, on changing the He/Ag/Pt(111) potential, a very different dependence, similar to that in the inset in Fig.5, is obtained (not shown here). Consequently, one would be forced to conclude that the fractal dimension changes when the interaction potential is varied. Within a simplistic interpretation, in which  $D$  is the *mass* fractal dimension, this is physically unacceptable. If, however, He measures the fractal dimension of the *electron density contours* – see Ref.[35] – a dependence on the potential is in fact expected. For mass fractals, analytical results have been obtained showing that the scattering intensities are self-affine functions, whose scaling exponent is simply related to the dimension of the scattering fractal sets.<sup>37</sup>

### C. Comparison of Experiments on Ag/Pt(111) with Scattering From Theoretical Disorder Models

In this final section we apply the understanding developed from the analysis of the various disorder models, to interpret He scattering data obtained in the experiments described in Sec.II A. To recapture the main details, the system studied in these experiments was a submonolayer of Ag at 50% coverage deposited on a Pt(111) surface at 38K. He scattering profiles were taken along the  $[11\bar{2}]$ -direction with incident wavenumber of  $6.43\text{\AA}^{-1}$ . The experimental data are the circles in Figs.8a-c (the same data is shown in all figures). Our purpose in performing the analysis to be described next was threefold: To *qualitatively* interpret the available experimental data and thus gain some understanding of the morphology of this low-temperature Ag/Pt(111) phase, to test the insight developed from the analysis of the disorder models, and to self-consistently test our empirically extracted potential.

If one focuses attention on the experimental data in, say, Fig.8b, several features (some of which observed in the previous sections) stand out:

1. Sharp specular and Bragg peaks, the latter having “shoulders”.
2. Off-specular structure manifested in oscillations of the intensity.
3. The *absence* (or at least masking) of specular peak broadening; instead clear maxima at  $-0.28, 0.37\text{\AA}^{-1}$  are present.
4. An asymmetry between positive and negative  $\Delta K$ .

The last point is an immediate consequence of the experimental scattering geometry, which breaks the left-right symmetry (see Sec.II A). This feature cannot be reproduced in the Sudden approximation calculations, in which the He always strikes the surface along its normal. The other observations can be used to reach several conclusions on the underlying surface structure:

- (1) The large compact clusters model [system (7)] cannot be ruled out since the broadening of the Bragg peaks is one of its main features.



(2) The presence of a series of peaks does not agree well with a fractal structure, which should exhibit a rather smooth decay of the intensity. Instead, one observes in Fig.8b that the scattering pattern from a 50% coverage fractal does contain peaks, for  $\Delta K < 3\text{\AA}^{-1}$ . The reason is that at such high coverage part of the fractal character is lost: adatoms fill in the gaps typical of the low coverage fractals of Fig.7, and the resulting surface structure is at first sight not very different from the random one of Fig.8a. However, the scattering intensities are markedly different in Figs.8a and b: the intensity decay in the fractal case is far smoother than in the random one, in agreement with the absence of a typical length scale ( $> a$ ) in the fractal. Point 2. then, can be used to eliminate both the fractal and randomly adsorbed adatom models: the former due to a lack of peak structure for  $\Delta K > 3\text{\AA}^{-1}$ , in the latter due to a complete disagreement in peak positions.

(3) The maxima adjacent to the specular are a feature which was absent in the disorder models we studied. They are most likely a result of constructive interference due to a length scale of  $\sim (2\pi/0.33)$ , i.e. about 4 lattice constants ( $19/(2.77\sqrt{3})$ ) along the  $[11\bar{2}]$  direction. At present we do not yet have a satisfactory model which contains such a length scale and is also in agreement with the other features of the intensity distribution.

Having essentially ruled out the fractal and random adatoms models, what then is an appropriate model which can at least qualitatively explain the features observed in the experimental intensities?<sup>38</sup> The central clue in answering this question is the off-specular peak structure. In the absence of agreement with the above models, we attempted a fit with a hybrid of the large compact islands and SCC model, namely a narrow *distribution* of translationally random small compact clusters. The advantage of this model is that it turns out that the positions and intensities of the off-specular peaks are extremely sensitive to the relative numbers and absolute diameters of these clusters. Thus a possible, although definitely not final morphological identification, is given in Fig.8c. The distribution shown is a set of hexagonal islands, 7 or 9 Ag atoms in diameter, mixed in a 1:4 ratio at 50% coverage. Upon a careful examination it will be noticed that apart from the quantitative location of the peaks near the specular discussed above, and the elevated intensity around the first order

Bragg, the positions of all other peaks are correctly reproduced (some of these peaks are mere shoulders in the experimental data; e.g. at  $3.0$  and  $4.6\text{\AA}^{-1}$ ). This agreement is not present in either the random adatom or fractal cases. On the other hand, the two missing features in the intensity pattern of Fig.8c seem likely to be explained by the introduction of some degree of *positional order* in the locations of the SCCs: A separation of about  $20\text{-}30\text{\AA}$  between the centers of every pair of adjacent clusters would result in the observed peaks, while at the same time create a shoulder underneath the Bragg peaks due to a slit-Fraunhofer effect [as for system (7)]. Such an ordered separation is in agreement with the fact that due to the size-mismatch between Pt and Ag, a strain is induced by the formation of an Ag island, resulting in an effective repulsion between neighboring islands. We observe evidence for this in the location of the experimental first order Bragg peak, which is located slightly below the position of the corresponding pure Pt(111) peak, suggesting some degree of lattice ordering due to Ag (which has a lattice constant of  $2.89\text{\AA}$ ). In addition there are some purely kinetic effects determining the size and distribution of islands, namely nucleation and an average diffusion length. The generation of a size-dispersed SCCs distribution satisfying the separation requirement turns out, however, to be a non-trivial task, and for the present qualitative purposes, we limit ourselves to the translationally random model. Beyond the introduction of positional order, one should probably also relax the assumption of perfect hexagons: At the low surface temperature considered, the mobility of Ag adatoms is extremely small, and consequently a more realistic model is probably one in which the hexagons are imperfect at least along their perimeter. Since the hexagons are perfect in our model, one observes an oscillation in the calculated intensity of Fig.8c, with a period of  $\sim 0.25\text{\AA}^{-1}$ ; this is likely due to interference between adatoms separated by 4-5 lattice constants along the chains making up the edges of the hexagons. At any rate, while clearly not being fully quantitative, the fit with the narrowly size-distributed SCCs is very promising and bound to be non-accidental.

#### IV. CONCLUDING REMARKS

The motivation for the study presented in this paper is the rapidly growing interest in structures formed on surfaces during epitaxial growth. We demonstrated that various types of disordered structures thus formed can be studied quantitatively by He scattering, and that a distinction between them can be made on the basis of the different scattering features that arise respectively in these cases. This is due to the high sensitivity of the He angular intensity spectrum to the surface morphology and electron distribution. In particular, we inverted a He/Ag/Pt(111) potential from experimental cross section measurements, and subsequently used this potential to predict from the analysis of experimental angular intensity data the presence of a phase of small and compact, narrowly size-dispersed clusters with some degree of positional order. The sensitivity to changes in both potential and morphology parameters of our fit to the experimental data, as well as support from a more general He-scattering study<sup>39</sup> and independent STM data,<sup>40</sup> provides strong evidence for the existence of this phase. Furthermore, it illustrates what we believe to be an important principle in surface science: The *combination* of the mutually complementary experimental (He scattering and STM) and theoretical techniques provides an extremely powerful tool for the quantitative analysis of complex surface structures.

Our theoretical findings shed light on several other points:

1. There are clear and specific differences between the intensity distributions resulting from the scattering from different classes of disordered structures. Careful analysis of the relevant features, such as broadening of the specular peak, the slope ( $d \log I / d \Delta K$ ), off-specular Fraunhofer maxima, position and width of Bragg peaks and more, can lead a long way to the identification of the type of disordered phase present on the surface.
2. The structure of the complex intensity spectrum obtained by scattering from translationally disordered, small compact clusters, can be understood as a sum of

the contributions due the scattering spectrum of a single such cluster, and due to the disorder. The former is mainly responsible for characteristic Fraunhofer and rainbow peaks in the large  $\Delta K$  regime, whereas the latter affects the slope of the intensity function for small  $\Delta K$  values and is responsible for the introduction of noise and peak “smearing”. Conversely, this information can be used to extract useful information about the individual cluster size and the cluster ensemble statistics.

3. The claim that for fractals the angular intensity dependence on parallel momentum transfer follows a universal power law, is not supported by our calculations. Instead there is a strong dependence on the parameters of the He/adsorbate potential. Thus it does not appear to be possible to calculate the fractal dimension from a simple scaling analysis of the intensity distribution.

Recent experimental studies have addressed the different kinds of disordered structures formed during 3D epitaxial growth. Specifically, the attenuation of the He scattering specular peak during growth was measured, allowing for the distinction between 2D vs. 3D growth mechanisms. The results presented here indicate that much more information on the structure of disordered multiple ad-layers can be obtained by He scattering, and we are currently pursuing such work.

### ACKNOWLEDGEMENTS

This work was supported by Grant No. I-215-006.5/91 from the German-Israel Foundation for Scientific Research (G.I.F.) to R.B.G. and G.C. The Fritz Haber Research Center at the Hebrew University is supported by the Minerva Gesellschaft für die Forschung mbH, München, Germany. The research was supported in part by the Institute of Surface and Interface Science at U.C. Irvine.

## APPENDIX

We derive Eq.(15). This requires first the evaluation of Eq.(14). The task at hand is the calculation of the probabilities  $\Pr(z_j; \vec{R}_1, \vec{R}_2)$ , to observe a given height difference between points located at  $\vec{R}_1$  and  $\vec{R}_2$  on the surface. Denoting the underlying surface as 0 and the atom tops as 1, there exist four possibilities:

- (1)  $\vec{R}_1, \vec{R}_2 \in 0$  with  $Z(\vec{R}_1, \vec{R}_2) = 0$ ;
- (2)  $\vec{R}_1 \in 0, \vec{R}_2 \in 1$  with  $Z(\vec{R}_1, \vec{R}_2) = h$ ;
- (3)  $\vec{R}_1 \in 1, \vec{R}_2 \in 0$  with  $Z(\vec{R}_1, \vec{R}_2) = -h$  and
- (4)  $\vec{R}_1, \vec{R}_2 \in 1$  with  $Z(\vec{R}_1, \vec{R}_2) = 0$ .

Denote  $S_{\epsilon_{\vec{R}_1} \epsilon_{\vec{R}_2}}$  (with  $\epsilon_{\vec{R}_i} = 0, 1$  according as to whether  $\vec{R}_i \in 0$  or  $\vec{R}_i \in 1$ ), as the probability of observing the point  $\vec{R}_1$  in phase  $\epsilon_{\vec{R}_1}$  and the point  $\vec{R}_2$  in phase  $\epsilon_{\vec{R}_2}$ . Then clearly:

$$\Pr(0; \vec{R}_1, \vec{R}_2) = S_{00} + S_{11} \quad \Pr(h; \vec{R}_1, \vec{R}_2) = S_{01} \quad \Pr(-h; \vec{R}_1, \vec{R}_2) = S_{10} \quad (17)$$

A general formalism for the evaluation of quantities of the type  $S_{\epsilon_{\vec{R}_1} \epsilon_{\vec{R}_2} \dots \epsilon_{\vec{R}_n}}$  is given by Torquato and Stell (TS).<sup>41</sup> Their result for the case of interest to us is:

$$S_n(\vec{R}_1, \dots, \vec{R}_n) = 1 + \sum_{k=1}^N \frac{(-\rho)^k}{k!} \int \dots \int g_k(\vec{x}^k) \prod_{j=1}^k \left( \left[ 1 - \prod_{i=1}^n (1 - m(|\vec{R}_i - \vec{x}_j|)) \right] \right) d\vec{x}_j \quad (18)$$

$$S_{11}(\vec{R}_1, \vec{R}_2) = 1 - (S_1(\vec{R}_1) + S_1(\vec{R}_2)) + S_{00}(\vec{R}_1, \vec{R}_2) \quad (19)$$

$$S_{01}(\vec{R}_1, \vec{R}_2) = S_1(\vec{R}_1) - S_{00}(\vec{R}_1, \vec{R}_2) \quad (20)$$

$$S_{10}(\vec{R}_1, \vec{R}_2) = S_1(\vec{R}_2) - S_{00}(\vec{R}_1, \vec{R}_2) \quad (21)$$

where  $S_n$  is shorthand for  $n$  points in phase 0 (so e.g.  $S_1$  above means one point in phase 0),  $\rho = N/A$  is the adsorbate density,  $\vec{x}^k \equiv (\vec{x}_1, \dots, \vec{x}_k)$ , and  $g_k$  is the reduced distribution function of  $k$  particles, defined as:

$$g_k(\vec{x}^k) = \frac{\rho_k(\vec{x}^k)}{\rho^k} \quad (22)$$

$$\rho_k(\vec{x}^k) = \frac{N!}{(N-k)!} P_k(\vec{x}^k) \quad (23)$$

$$P_k(\vec{x}^k) = \int \dots \int P(\vec{x}_1, \dots, \vec{x}_N) d\vec{x}_{k+1} \dots d\vec{x}_N. \quad (24)$$

In the case of an isotropic system  $g_2(\vec{x}_1, \vec{x}_2) = g(r)$  (where  $r = |\vec{x}_1 - \vec{x}_2|$ ) is the well-known radial distribution function. The function  $m(|\vec{R}_i - \vec{x}_j|)$  is the “particle indicator function”, defined as:

$$m(|\vec{R} - \vec{x}_j|) = \begin{cases} 1 & \text{if } |\vec{R} - \vec{x}_j| < d/2 \\ 0 & \text{if } |\vec{R} - \vec{x}_j| > d/2. \end{cases} \quad (25)$$

Collecting Eqs.(11),(14),(17), we obtain:

$$I(\Delta\vec{K}) = \frac{1}{A^2} \int d\vec{R}_1 d\vec{R}_2 e^{i\Delta\vec{K}\cdot(\vec{R}_1 - \vec{R}_2)} \times \\ \left[ (S_{00}(\vec{R}_1, \vec{R}_2) + S_{11}(\vec{R}_1, \vec{R}_2)) + e^{2ihk_z} S_{01}(\vec{R}_1, \vec{R}_2) + e^{-2ihk_z} S_{10}(\vec{R}_1, \vec{R}_2) \right]. \quad (26)$$

The last equation, together with Eqs.(18)-(24), establish a formal connection between the reduced distribution functions of interest in characterization of surface statistics and the measurable scattering intensity.

Eq.(26) can next be applied to the scattering from translationally random adatoms. It is shown by TS that in this case, since  $g_k \equiv 1$  for all  $k$ , one obtains:

$$S_n(\vec{R}_1, \dots, \vec{R}_n) = e^{-\rho V_n(\vec{R}^n; d)}, \quad (27)$$

where  $V_n$  is the union area of  $n$  circles with diameter  $d$ , with centers at  $\{\vec{R}_1, \dots, \vec{R}_n\}$ . For  $n = 1, 2$  there exist explicit formulae:

$$V_1 = \frac{1}{4}\pi d^2 \quad (28)$$

$$V_2(R/d) = \frac{1}{2}\pi d^2 - \frac{1}{2}d^2 \left( \cos^{-1} \frac{R}{d} - \frac{R}{d} \sqrt{1 - \frac{R^2}{d^2}} \right) H(1 - R/d) \quad (29)$$

Here  $R = |\vec{R}_1 - \vec{R}_2|$  and  $H(x)$  is the Heavyside step function. Note that in the scattering context,  $d = d(k_z)$ ,  $d$  being the diameter of the cross-section, which depends on the incident He wavenumber  $k_z$ . Using this in Eqs.(27),(19)-(21), and recalling that the present system is translationally invariant, we obtain:

$$S_{00}(R/d) = e^{-\rho V_2(R/d)} \quad (30)$$

$$S_{11}(R/d) = 1 - 2e^{-\frac{1}{4}\rho\pi d^2} + e^{-\rho V_2(R/d)} \quad (31)$$

$$S_{01}(R/d) = S_{10}(R/d) = e^{-\frac{1}{4}\pi\rho d^2} - e^{-\rho V_2(R/d)} \quad (32)$$

What remains is to insert the last expressions into the general formula for the scattering intensity, Eq.(26), and go through some algebra and integrations. Defining:

$$\begin{aligned} \beta &= \rho d^2 \\ \gamma &= 2k_z h \\ \epsilon &= \frac{d^2}{A} \end{aligned} \quad (33)$$

and:

$$c_1(\beta, \gamma, A) = \frac{(2\pi)^2}{A} \left( 1 + 2e^{-\frac{1}{4}\pi\beta} (\cos(\gamma) - 1) \right) \quad (34)$$

$$c_2(\beta, \gamma, \epsilon) = 4\pi\epsilon(1 - \cos(\gamma)) e^{-\frac{1}{2}\pi\beta} \quad (35)$$

we obtain:

$$I(\Delta\vec{K}) = \frac{1}{(2\pi)^2} c_1 \int d\vec{R} e^{i\Delta\vec{K}\cdot\vec{R}} + \frac{e^{\frac{1}{2}\pi\beta}}{2\pi d^2} c_2 \int d\vec{R} e^{i\Delta\vec{K}\cdot\vec{R}} e^{-\rho V_2(R/d)} \quad (36)$$

The first integral evaluates to a delta-function, whereas the second simplifies to:

$$2\pi e^{-\frac{1}{2}\pi\beta} \left[ \int_0^d J_0(R \Delta K) e^{\frac{1}{2}\beta \left( \cos^{-1} \frac{R}{d} - \frac{R}{d} \sqrt{1 - \frac{R^2}{d^2}} \right)} R dR + \int_d^\infty J_0(R \Delta K) R dR \right]$$

Let us now define:

$$g(\alpha, \beta) = \int_0^1 J_0(\alpha S) e^{\frac{1}{2}\beta (\cos^{-1} S - S\sqrt{1-S^2})} S dS, \quad (37)$$

then finally the scattering intensity becomes:

$$I(\Delta\vec{K}) = \delta(\Delta\vec{K}) c_1(\beta, \gamma, A) + c_2(\beta, \gamma, \epsilon) \left[ g(\Delta K d, \beta) + \frac{J_{-1}(\Delta K d)}{\Delta K d} \right]. \quad (38)$$

## REFERENCES

- <sup>1</sup> S.C. Wang, G. Ehrlich, Surf. Sci. **239**, 301 (1990).
- <sup>2</sup> H. Brune, H. Röder, C. Boragno and K. Kern, Phys. Rev. Lett. **73**, 1955 (1994).
- <sup>3</sup> H. Röder, H. Brune, J.-P. Bucher and K. Kern, Surf. Sci. **298**, 121 (1993).
- <sup>4</sup> P. Zeppenfeld, M. Krzyzowski, Ch. Romainczyk, G. Comsa and M.G. Lagally, Phys. Rev. Lett. **72**, 2737 (1994).
- <sup>5</sup> G. Rosenfeld, A.F. Becker, B. Poelsema, L.K. Verheij and G. Comsa, Phys. Rev. Lett. **69**, 917 (1992).
- <sup>6</sup> R. Stumpf and M. Scheffler, Phys. Rev. Lett. **72**, 254 (1994).
- <sup>7</sup> P. Blandin, C. Massobrio and P. Ballone, Phys. Rev. B **49**, 48 (1994).
- <sup>8</sup> S. Esch, M. Hohage, T. Michely and G. Comsa, Phys. Rev. Lett. **72**, 518 (1994).
- <sup>9</sup> M. Yanuka, A.T. Yinnon, R.B. Gerber, P. Zeppenfeld, K. Kern, U. Becher and G. Comsa, J. Chem. Phys. **99**, 8280 (1993).
- <sup>10</sup> D.A. Hamburger, A.T. Yinnon, I. Farbman, A. Ben Shaul and R.B. Gerber, Surf. Sci. **327**, 165 (1995).
- <sup>11</sup> M. Bott, T. Michely and G. Comsa, Surf. Sci. **272**, 161 (1992).
- <sup>12</sup> P. Zeppenfeld, M. Krzyzowski, Ch. Romainczyk, R. David, G. Comsa, H. Röder, K. Bromann, H. Brune and K. Kern, Surf. Sci. Lett. **342**, L1131 (1995).
- <sup>13</sup> M. Krzyzowski, Ch. Romainczyk, P. Zeppenfeld, R. David and G. Comsa, to be published.
- <sup>14</sup> A.T. Yinnon, R. Kosloff, R.B. Gerber, B. Poelsema and G. Comsa, J. Chem. Phys. **88**, 3722 (1988).
- <sup>15</sup> A.F. Becker, G. Rosenfeld, B. Poelsema and G. Comsa, Phys. Rev. Lett. **70**, 477 (1993).



- <sup>16</sup> R. Schinke and R.B. Gerber, J. Chem. Phys. **82**, 1567 (1985).
- <sup>17</sup> R.B. Gerber, A.T. Yinnon, M. Yanuka, D. Chase, Surf. Sci., **272**, 81 (1992)
- <sup>18</sup> R. B. Gerber, Chem. Rev. **87**, 29 (1987).
- <sup>19</sup> H. C. Kang and W. H. Weinberg, Surf. Sci. **299/300**, 755 (1994).
- <sup>20</sup> H. C. Kang and W. H. Weinberg, Acc. Chem. Res. **25**, 253 (1992).
- <sup>21</sup> C. Uebing and R. Gomer, J. Chem. Phys., **95**, 7626 (1991).
- <sup>22</sup> R.B. Gerber, A.T. Yinnon and J.N. Murrell, J. Chem. Phys., **31**, 1 (1978).
- <sup>23</sup> A.T. Yinnon, R.B. Gerber, D.K. Dacol and H. Rabitz, J. Chem. Phys. **84**, 5955 (1986).
- <sup>24</sup> D.K. Dacol, H. Rabitz and R.B. Gerber, J. Chem. Phys. **86**, 1616 (1987).
- <sup>25</sup> R.B. Gerber, Delgado-Barrio, editor, in *Dynamics of Molecular Processes*, p.299, (IOP, Bristol, 1993).
- <sup>26</sup> B. Poelsema and G. Comsa, in *Scattering of Thermal Energy Atoms from Disordered Surfaces*, Springer Tracts in Modern Physics, Vol. 115 (Springer, Berlin, 1989).
- <sup>27</sup> A.T. Yinnon, R. Kosloff and R.B. Gerber, J. Chem. Phys. **88**, 7209 (1988).
- <sup>28</sup> D.A. Hamburger and R.B. Gerber, J. Chem. Phys. **102**, 6919 (1995).
- <sup>29</sup> In fact the potential was obtained for He/Pt(110), but should likewise be applicable to the Pt(111) face since the potential is a *laterally averaged* one.
- <sup>30</sup> M.A. Krzyzowski, P. Zeppenfeld and G. Comsa, J. Chem. Phys. **103**, 8705 (1995).
- <sup>31</sup> A.M. Lahee, J.P. Manson, J.P. Toennies and C. Wöll, J. Chem. Phys. **86**, 7194 (1987).
- <sup>32</sup> N. Esbjerg and J.K. Norskov, Phys. Rev. Lett. **45**, 807 (1980); N.D. Lang and J.K. Norskov, Phys. Rev. B **27**, 4612 (1983); J.K. Norskov, K.W. Norskov, P. Stoltze and L.B. Hansen, Surf. Sci. **283**, 277 (1993).

- <sup>33</sup> M. Bott, M. Hohage, M. Morgenstern, T. Michely and George Comsa, Phys. Rev. Lett. **76**, 1304 (1996)
- <sup>34</sup> H. Brune, C. Romainczyk, H. Röder, and K. Kern, Nature **369**, 469 (1994).
- <sup>35</sup> D.A. Hamburger, A.T. Yinnon and R.B. Gerber, Chem. Phys. Lett. **253**, 223 (1996)
- <sup>36</sup> P.Pfeifer and M.W. Cole, New J. of Chem. **14**, 221 (1990).
- <sup>37</sup> D.A. Hamburger-Lidar, Phys. Rev. E., **54**, 354 (1996).
- <sup>38</sup> It may be appropriate at this point to explain why we did not use the KMC method to generate configurations at 38K to guide us in the search for a model for the surface morphology. The reason is that, as explained in Sec.IIB1, we do not have an absolute temperature scale available in the KMC simulations.
- <sup>39</sup> M.A. Krzyzowski, P. Zeppenfeld and G. Comsa, to be published.
- <sup>40</sup> H. Röder, thesis Nr. 1288, EPF Lausanne (1994).
- <sup>41</sup> S. Torquato and G. Stell, J. Chem. Phys. **77**, 2071 (1982); **78**, 3262 (1983); **79**, 1505 (1983).

## FIGURES

FIG. 1. A comparison between experimental and theoretical cross-sections for He scattered from an isolated Ag atom adsorbed on a Pt(111) surface. The experimental values were determined from adsorption curves  $I(\Theta)$  (Eq.(6)) recorded at 38K and extrapolated to  $\Theta \rightarrow 0$ . A fit (solid line) of the theoretical cross-sections was used to derive the potential used in this work.

FIG. 2. Calculated angular intensity distribution along the  $\Gamma_K$  direction for He scattered from an ordered monolayer of Ag on the Pt(111) surface, with the Ag/Pt(111) lattice mismatch ignored. The orientation of the scattering plane is along the close packed  $[1\bar{1}0]$  direction in real space. The reciprocal space lattice is rotated by  $30^\circ$  so that the Bragg peaks appear at non-close packed multiples of  $4\pi/a$ ,  $a = 2.77\text{\AA}$  being the Pt(111) lattice constant. For the indexing of the Bragg peaks, we chose real space unit vectors  $\vec{a}_1 = (a/2, \sqrt{3}a/2)$ ,  $\vec{a}_2 = (-a/2, \sqrt{3}a/2)$ , corresponding to reciprocal space unit vectors  $\vec{b}_1 = (2\pi/a)(1, 1/\sqrt{3})$ ,  $\vec{b}_2 = (2\pi/a)(1, -1/\sqrt{3})$ .

FIG. 3. Dashed line: Calculated angular intensity distribution along the  $\Gamma_K$  direction of He scattered from a single Ag adatom. Solid line: Same for He scattered from 15% coverage translationally random Ag atoms on a Pt(111) lattice.

FIG. 4. Dashed line: Calculated angular intensity distribution along the  $\Gamma_K$  direction of He scattered from a single Ag heptamer. Solid line: Same for He scattered from randomly distributed Ag heptamers on Pt(111). Inset: Top view of a small compact cluster (heptamer).

FIG. 5. Calculated angular intensity distribution of He scattered from a Pt(111) surface with 15% adsorbed Ag atoms with off-lattice translational randomness. Thin line: Sudden approximation results. Thick lines: calculation using Eq.(15). Right Inset: Same, using a harder He/Ag potential. Left inset: The disorder term  $g$  compared to the single adatom term, from Eq.(15) (linear scale).

FIG. 6. Calculated angular intensity distribution of He scattered along the  $\Gamma_K$  direction from randomly distributed large compact Ag islands on Pt(111). Inset: Compact Ag islands produced by a KMC simulation, at 15% coverage on a surface of  $100 \times 100$  unit cells and  $T=500\text{K}$ . The surface is a parallelogram with an angle of  $60^\circ$ . Periodic boundary conditions are employed, so straight edges usually imply that the cluster is continued at the opposite boundary.

FIG. 7. Calculated angular intensity distribution of He scattered along the  $\Gamma_K$  direction from a Pt(111) surface with 15% adsorbed Ag atoms, forming fractal islands. Left inset: KMC simulations as in Fig.6, but for fractal islands ( $T=200\text{K}$ ). Right Inset: Power-law regression of the intensity (see text for details).

FIG. 8. A comparison between experimental and theoretical angular intensities for He scattered from a Pt(111) surface with 50% adsorbed Ag atoms in different disorder classes: (a) Translationally random adatoms, (b) Fractal islands, (c) Size-dispersed compact islands. Insets: Typical configurations in each of the disorder classes. The orientation of the scattering plane is along the non-close packed  $[11\bar{2}]$  direction in real space, corresponding to the close packed  $\Gamma_M$  direction in reciprocal space. Thus Bragg peaks appear at multiples of  $4\pi/(\sqrt{3}a)$  where  $a = 2.77\text{\AA}$  is the Pt(111) lattice constant. Experimental surface temperature: 38K, He beam energy: 21.6meV ( $k_z = 6.43\text{\AA}^{-1}$ ). Solid lines: theoretical intensities. Circles: experimental data. Note that only the elastically scattered intensity is shown. The inelastic part was separated in the experiment using time-of-flight spectroscopy.

Fig. 1

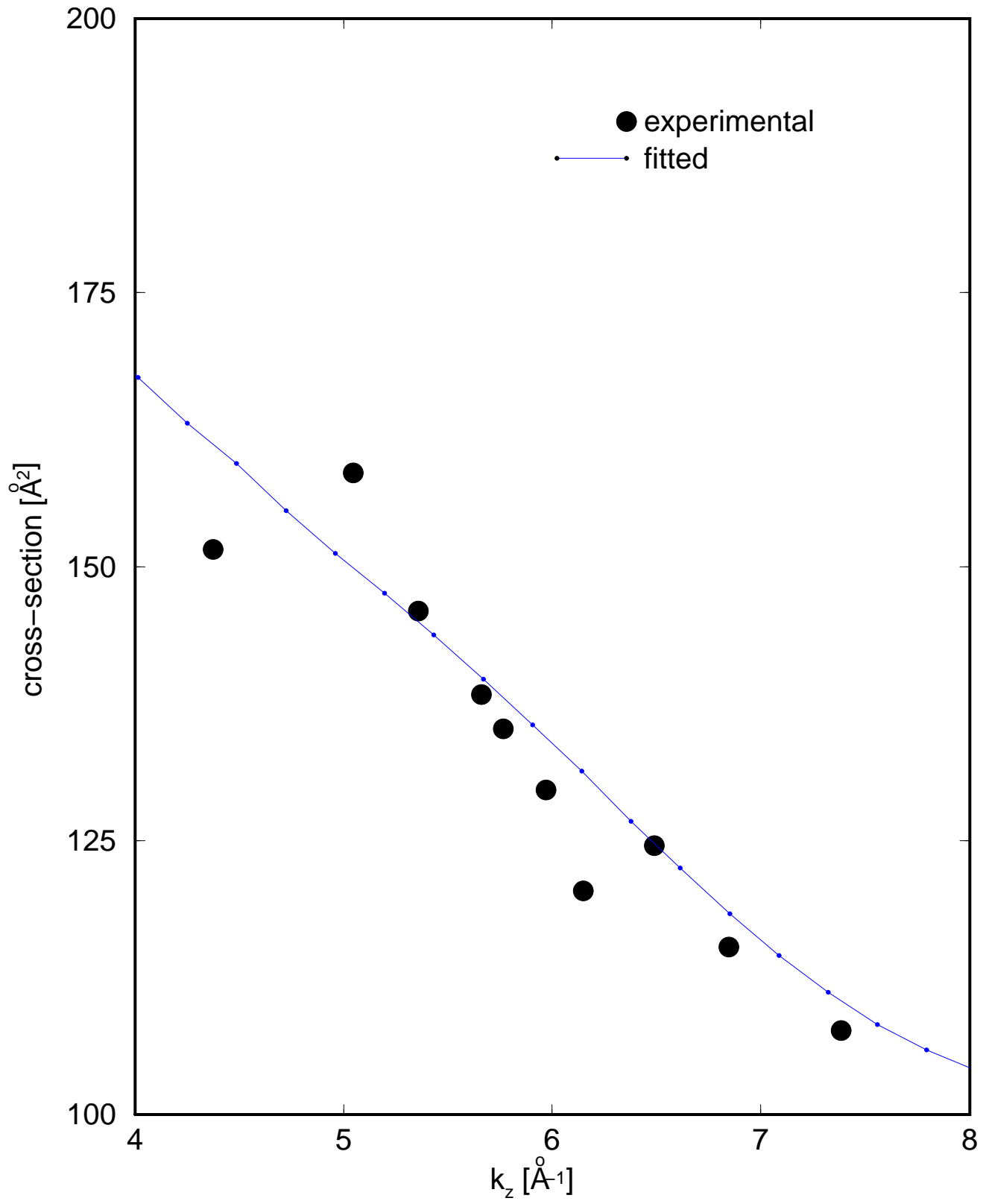


Fig. 2

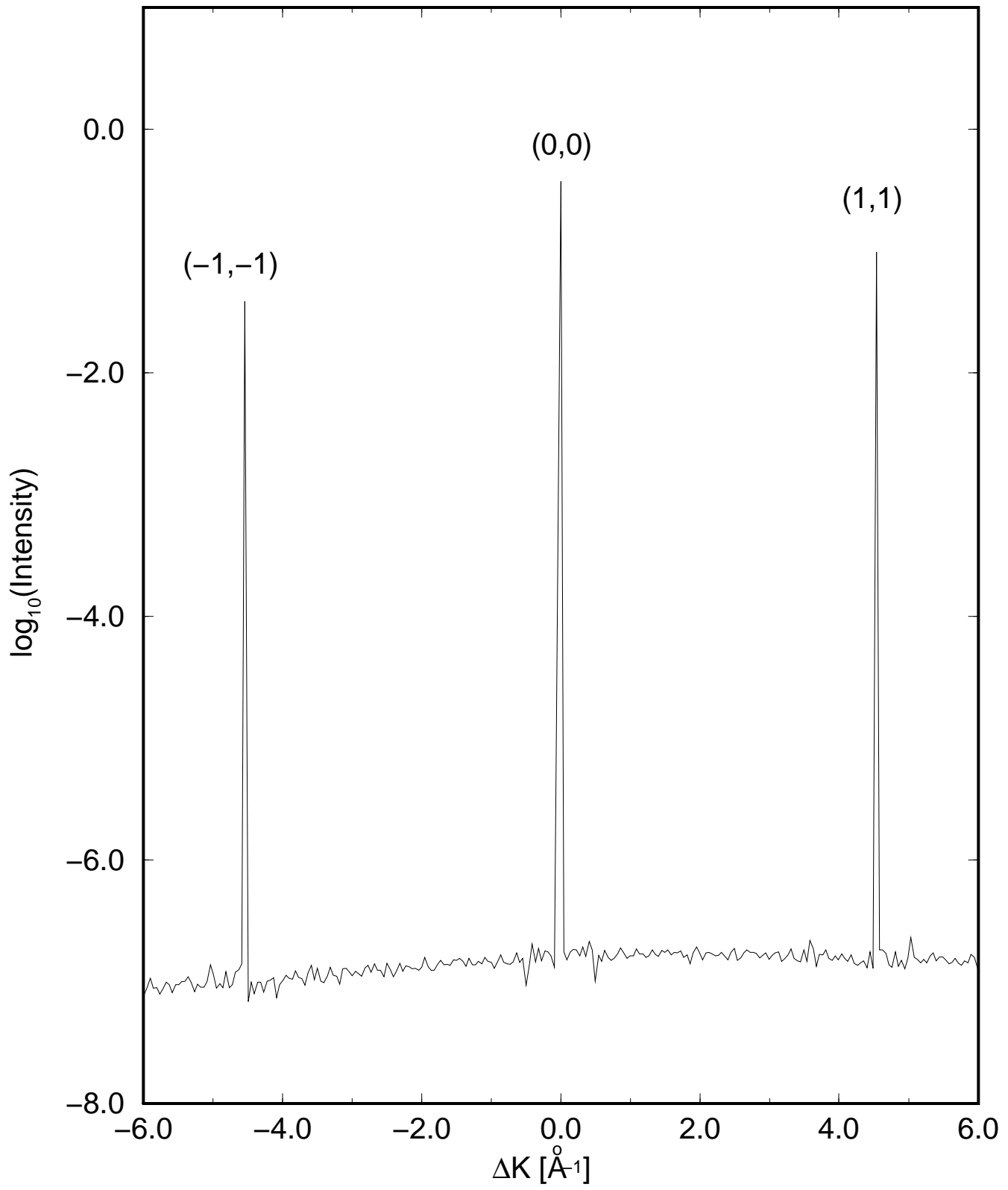


Fig. 3

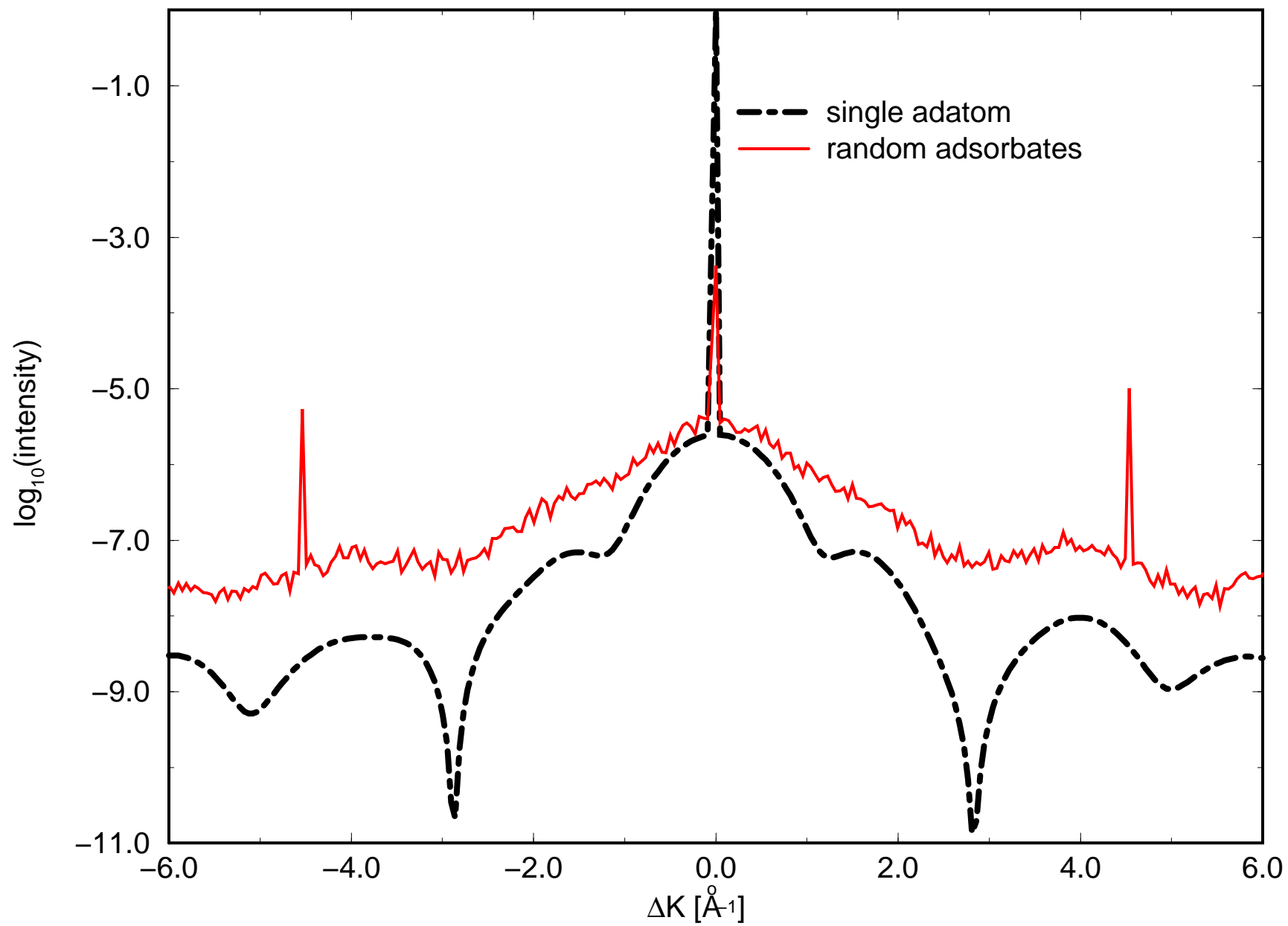


Fig. 4

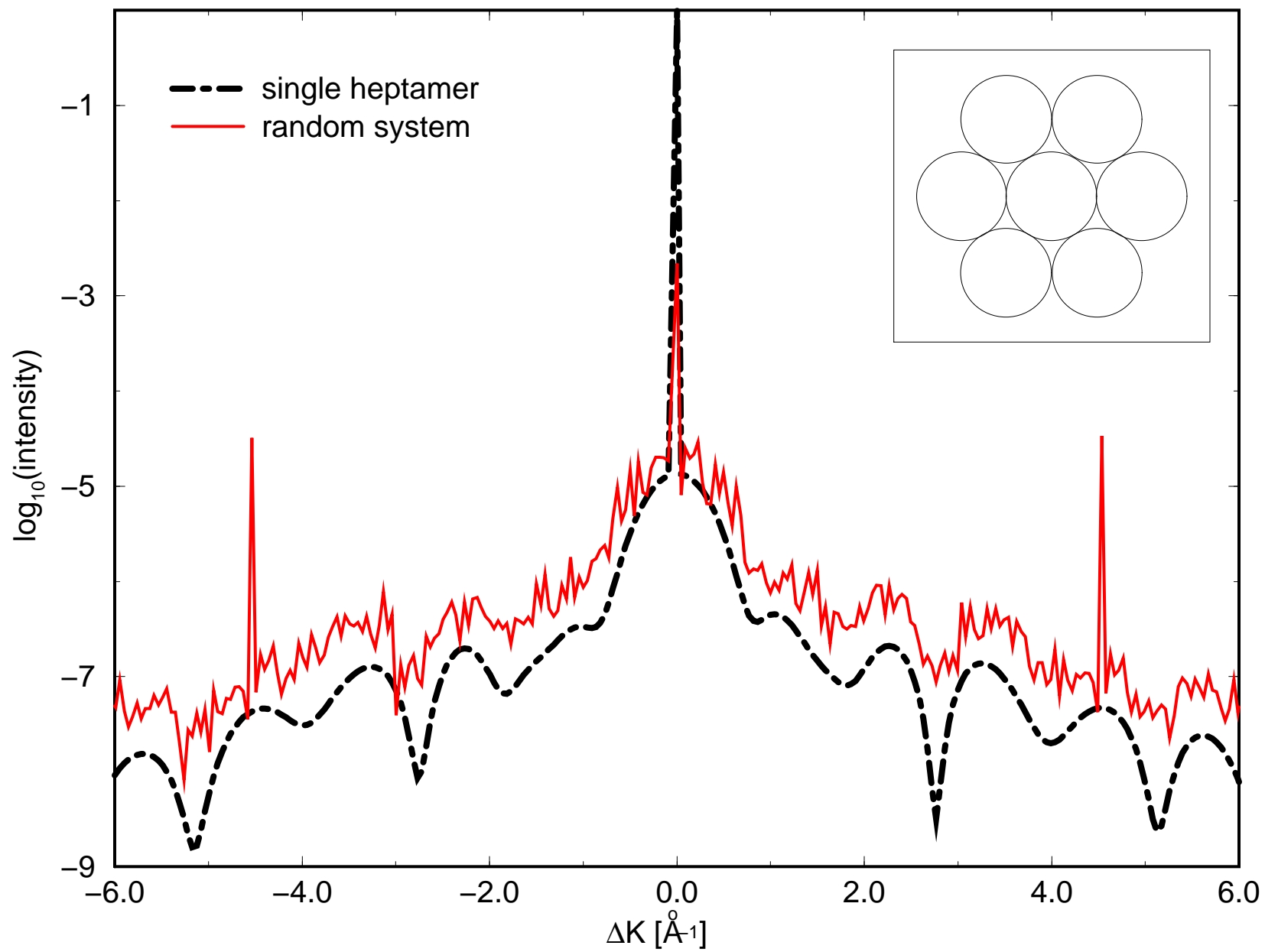




Fig. 5

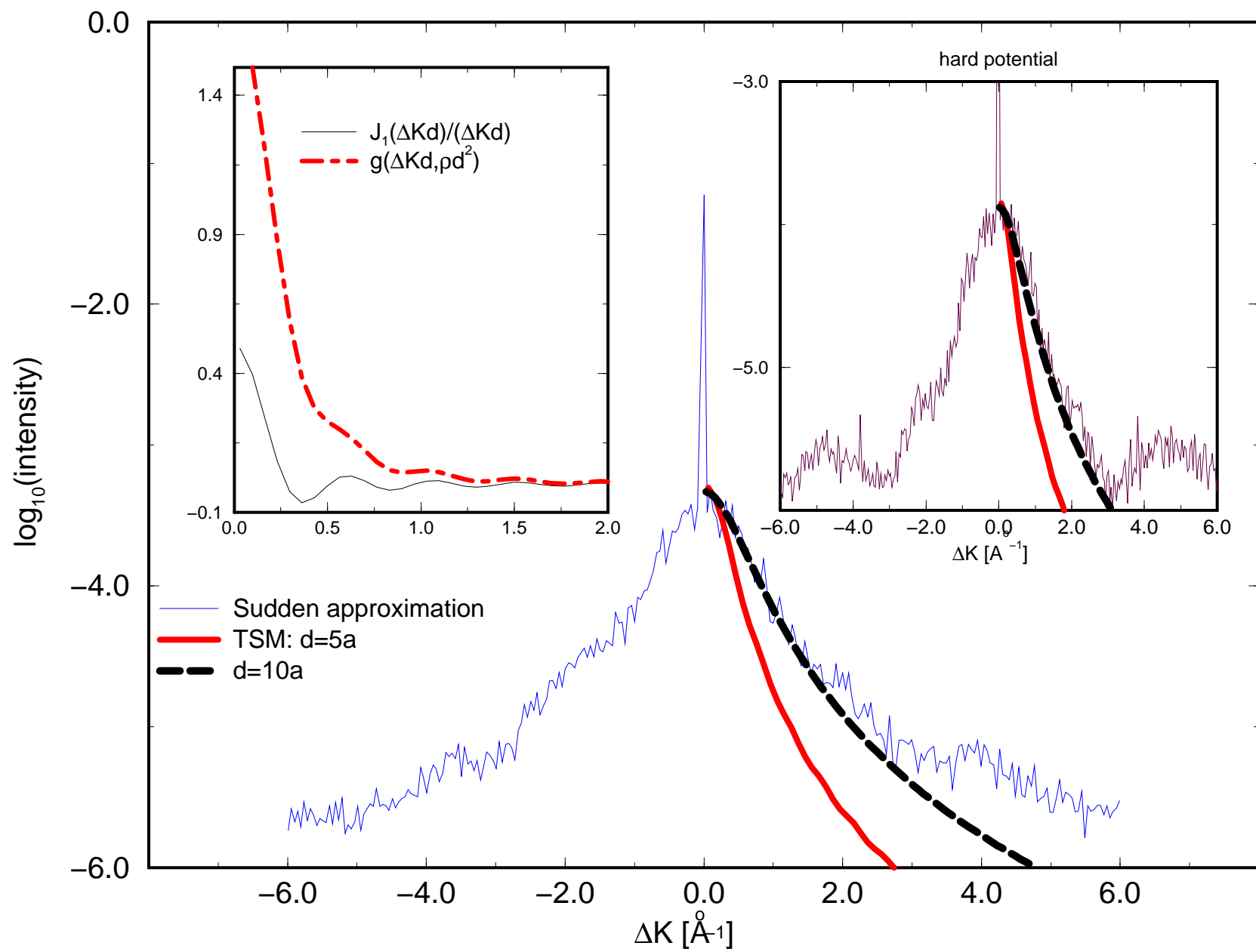


Fig. 6

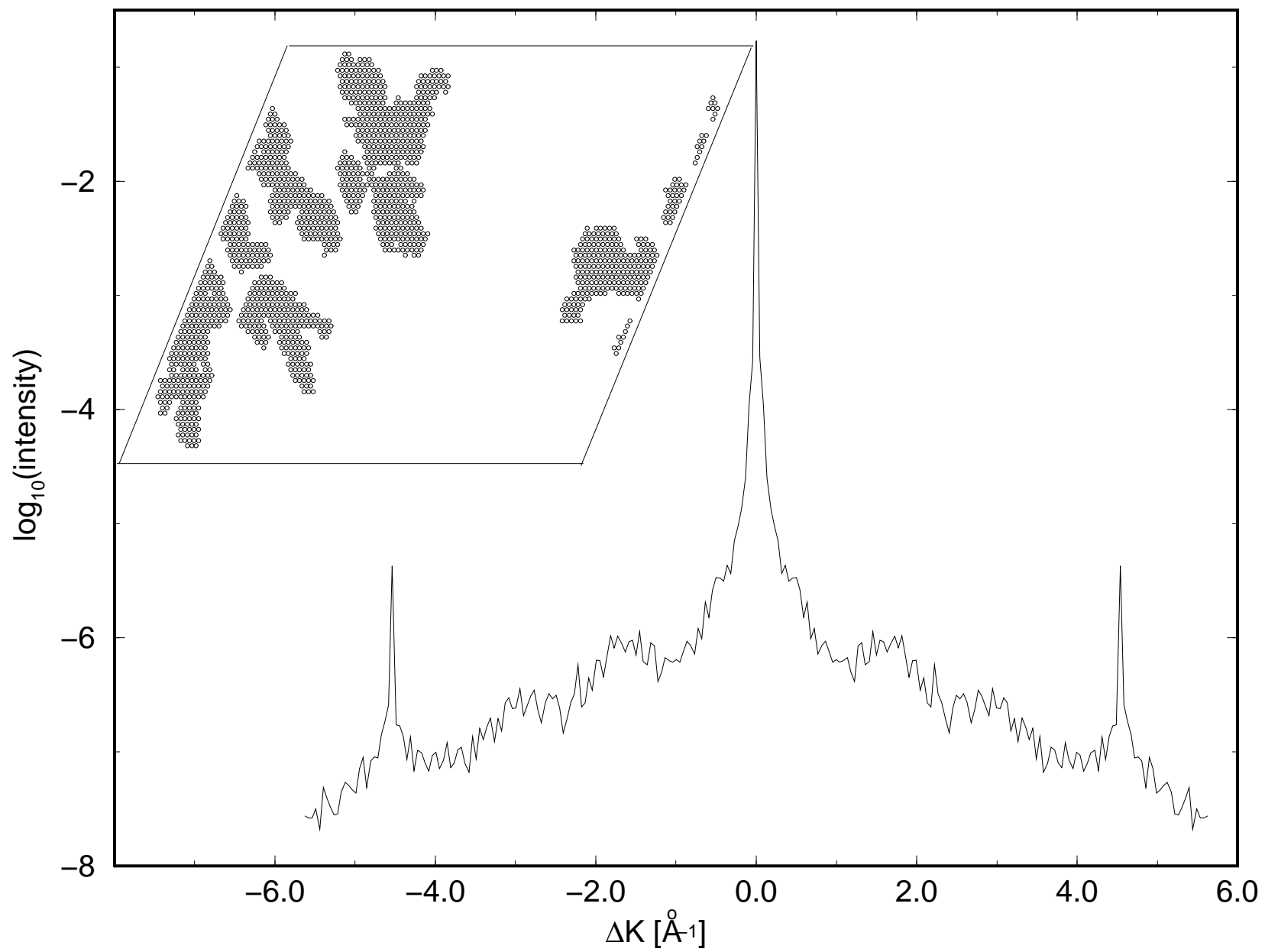


Fig. 7

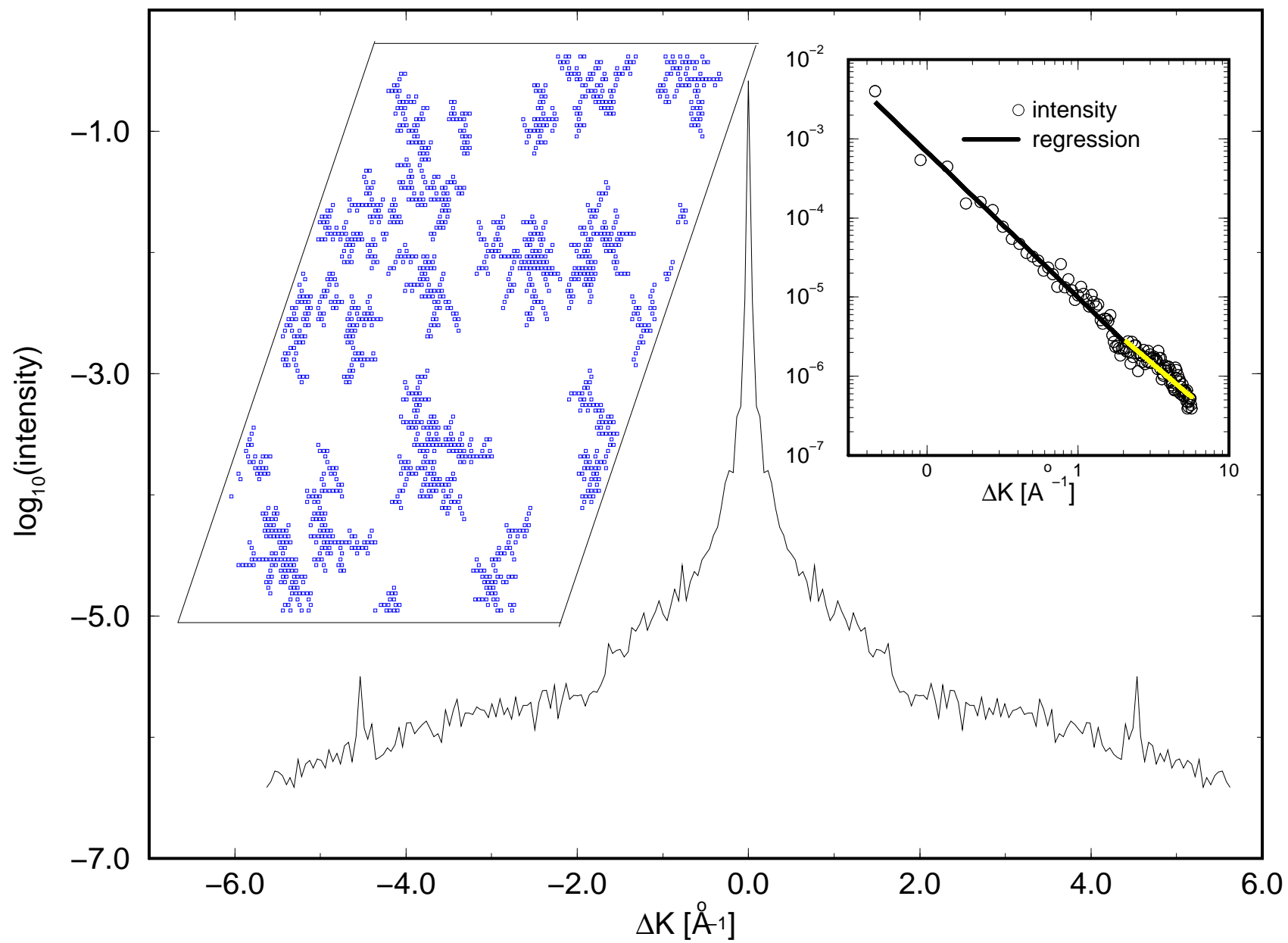


Fig. 8a

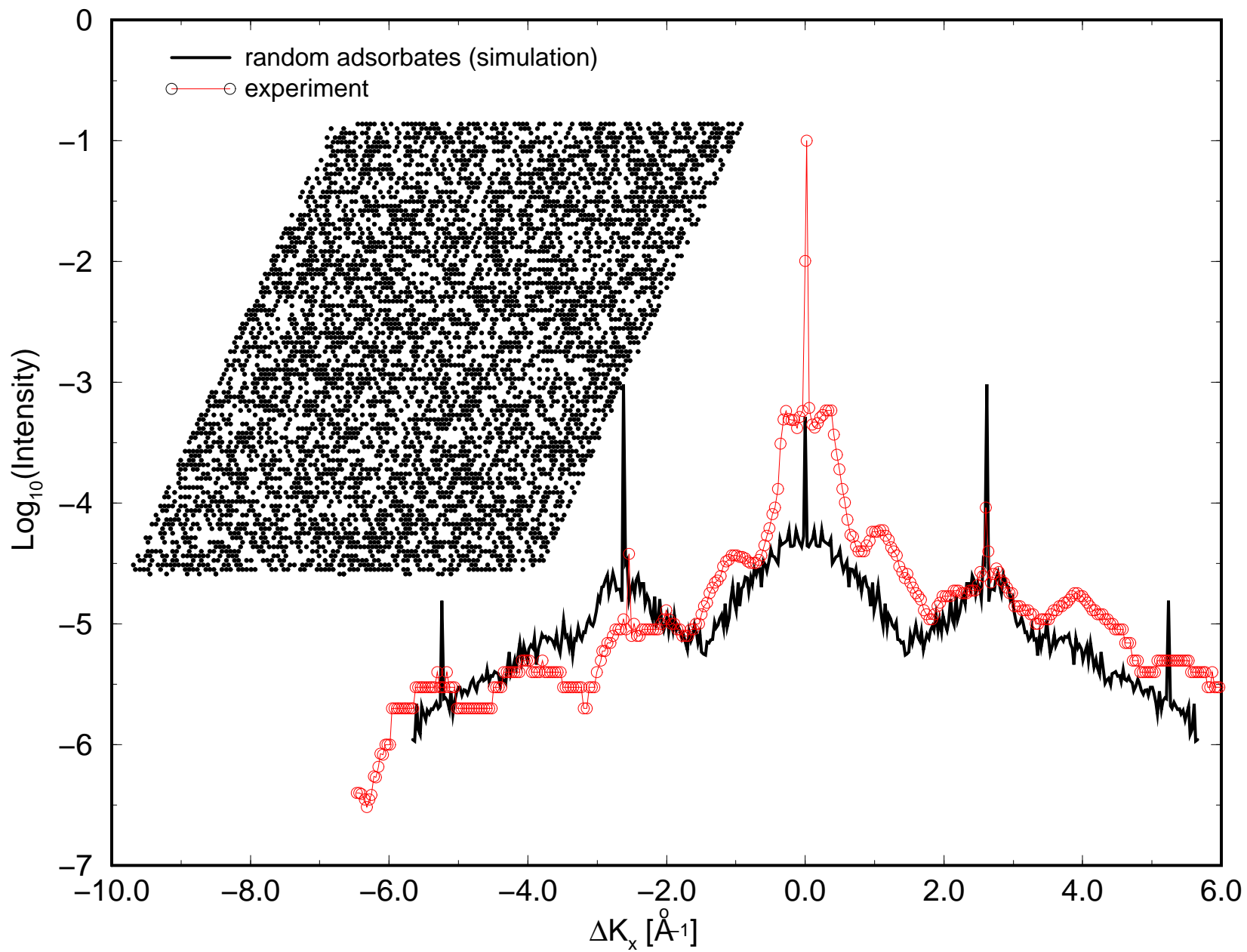


Fig. 8b

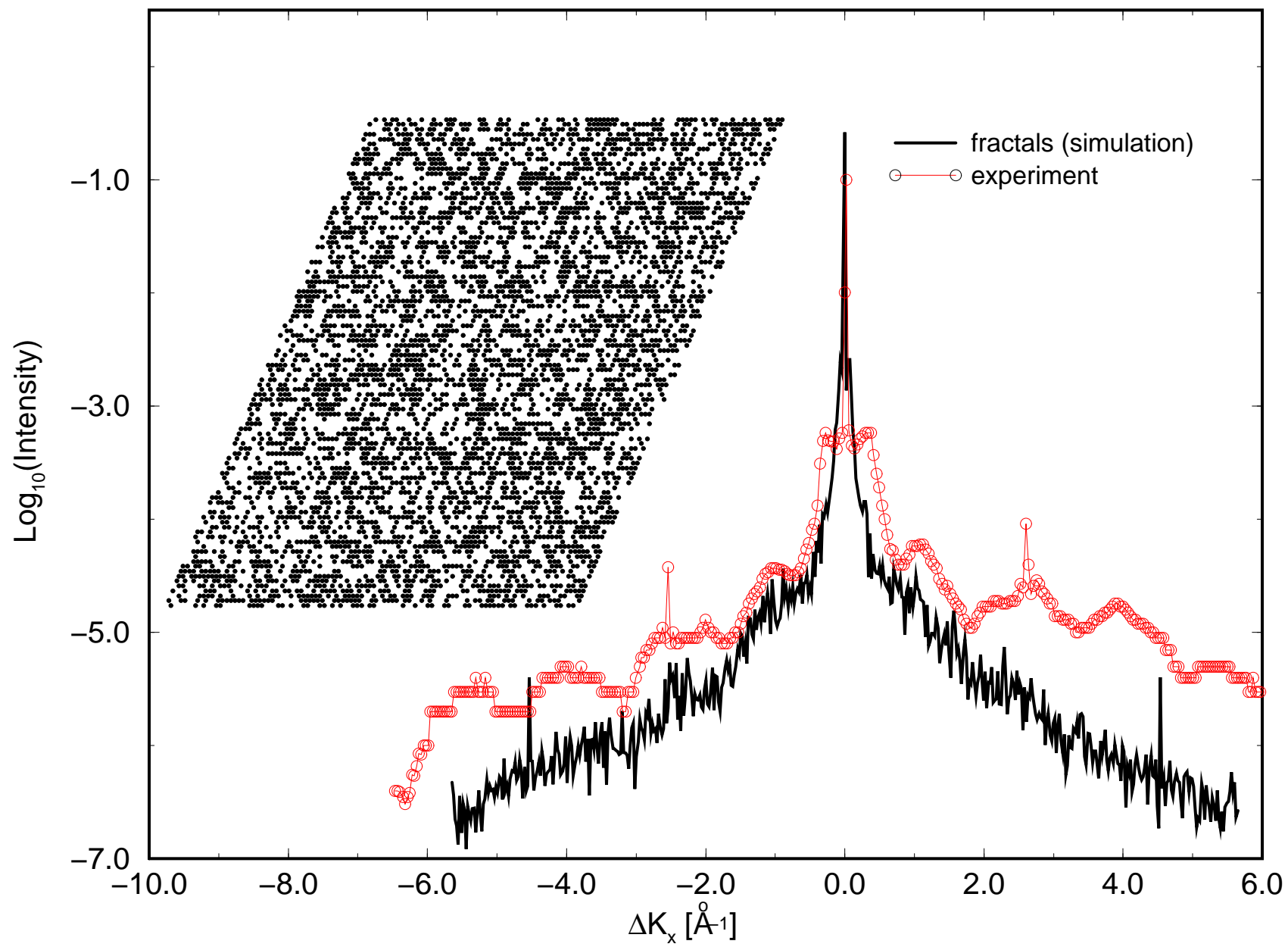


Fig. 8c

